






REPORT

# Coupled sterol synthesis and transport machineries at ER–endocytic contact sites

Javier Encinar del Dedo , Isabel María Fernández-Golbano, Laura Pastor , Paula Meler , Cristina Ferrer-Orta, Elena Rebollo , and Maria Isabel Geli 

**Sterols are unevenly distributed within cellular membranes. How their biosynthetic and transport machineries are organized to generate heterogeneity is largely unknown. We previously showed that the yeast sterol transporter Osh2 is recruited to endoplasmic reticulum (ER)–endocytic contacts to facilitate actin polymerization. We now find that a subset of sterol biosynthetic enzymes also localizes at these contacts and interacts with Osh2 and the endocytic machinery. Following the sterol dynamics, we show that Osh2 extracts sterols from these subdomains, which we name ERSEs (ER sterol exit sites). Further, we demonstrate that coupling of the sterol synthesis and transport machineries is required for endocytosis in mother cells, but not in daughters, where plasma membrane loading with accessible sterols and endocytosis are linked to secretion.**

## Introduction

A pronounced heterogeneity in the sterol content of cellular membranes is maintained (Menon, 2018; Mesmin et al., 2013). How such heterogeneity is generated, and how it contributes to particular functions, is fairly unknown. Despite sterols are synthesized at the ER, their level in this compartment is kept low (Mesmin et al., 2013). This implies that sterol synthesis and extraction must be coupled. Nonvesicular sterol transport is thought to convey ER sterols to the plasma membrane (PM) in yeast (Baumann et al., 2005), but detailed information on the sterol routes is missing. Proteins with capacity to transfer sterols include OSBP (oxysterol-binding protein)-related proteins (ORPs; Wong et al., 2019). In yeast, *OSH1* to *OSH7* encode ORP-like proteins. Osh1, Osh2, Osh4, and Osh5 extract sterols in vitro (Raychaudhuri et al., 2006; Schulz et al., 2009), whereas Osh6 and Osh7 transport phosphatidylserine (Maeda et al., 2013). Oshes are thought to counter-transport phosphatidylinositol-4 phosphate (PI4P) to fuel lipid transport against gradient (de Saint-Jean et al., 2011; Moser von Filseck et al., 2015b), but direct in vivo evidence for the hypothesis is missing for many Oshes. Oshes localize at specialized membrane contact sites (MCSs; Prinz et al., 2020; Wong et al., 2019), where they sustain different processes (Beh et al., 2001). In this context, we found that Osh2 and Osh3 are components of ER–endocytic MCSs (Encinar del Dedo et al., 2017). Contact of the ER with endocytic sites promotes actin polymerization and membrane invagination (Encinar del Dedo et al., 2017). Endocytosis in yeast requires sterols, and the endocytic function of Osh2 depends on its sterol transfer activity (Encinar del Dedo et al., 2017; Maeda et al., 2013;

Moser von Filseck et al., 2015a). Thus, Osh2 could locally transfer sterols from the ER to endocytic sites, but the functional need for this transport is difficult to reconcile with the high levels of sterols at the PM (Menon, 2018; Schneiter et al., 1999). Nonetheless, one must take into account that the pool of active cytosolic-accessible sterol is tuned not only by its concentration but also by the membrane composition and curvature (Menon, 2018; Mesmin et al., 2013; Moser von Filseck et al., 2015b).

Here, we followed the sterol dynamics in yeast with the D4H domain of perfringolysin (PFO), which only binds sterols when its C3 hydroxyl group is exposed (Maekawa, 2017; Savinov and Heuck, 2017). We found that accessible sterols were highly polarized, accumulating at the PM of daughter cells. In mothers, the probe was instead recruited to ER subdomains labeled with a subset of sterol biosynthetic enzymes (Ergs), which also interacted with Myo5 and Osh2. Further, we showed that Osh2 extracts sterols from these subdomains, which we name ERSEs (ER sterol exit sites). Finally, we found that although sterols are critical for endocytosis, on-site coupling of the sterol synthesis and transport machineries was needed in mother cells, but not in daughters, where endocytosis and PM loading with sterols were linked to secretion.

## Results and discussion

### Yeast cytosolic-accessible sterols are polarized

To investigate the dynamics of cytosolic-accessible sterols in yeast, we expressed GFP-D4H (Johnson et al., 2012; Koselny

.....  
 Institute for Molecular Biology of Barcelona, Spanish Research Council, Barcelona, Spain.

Correspondence to Maria Isabel Geli: [mgfbmc@ibmb.csic.es](mailto:mgfbmc@ibmb.csic.es).

© 2021 Encinar del Dedo et al. This article is distributed under the terms of an Attribution–Noncommercial–Share Alike–No Mirror Sites license for the first six months after the publication date (see <http://www.rupress.org/terms/>). After six months it is available under a Creative Commons License (Attribution–Noncommercial–Share Alike 4.0 International license, as described at <https://creativecommons.org/licenses/by-nc-sa/4.0/>).

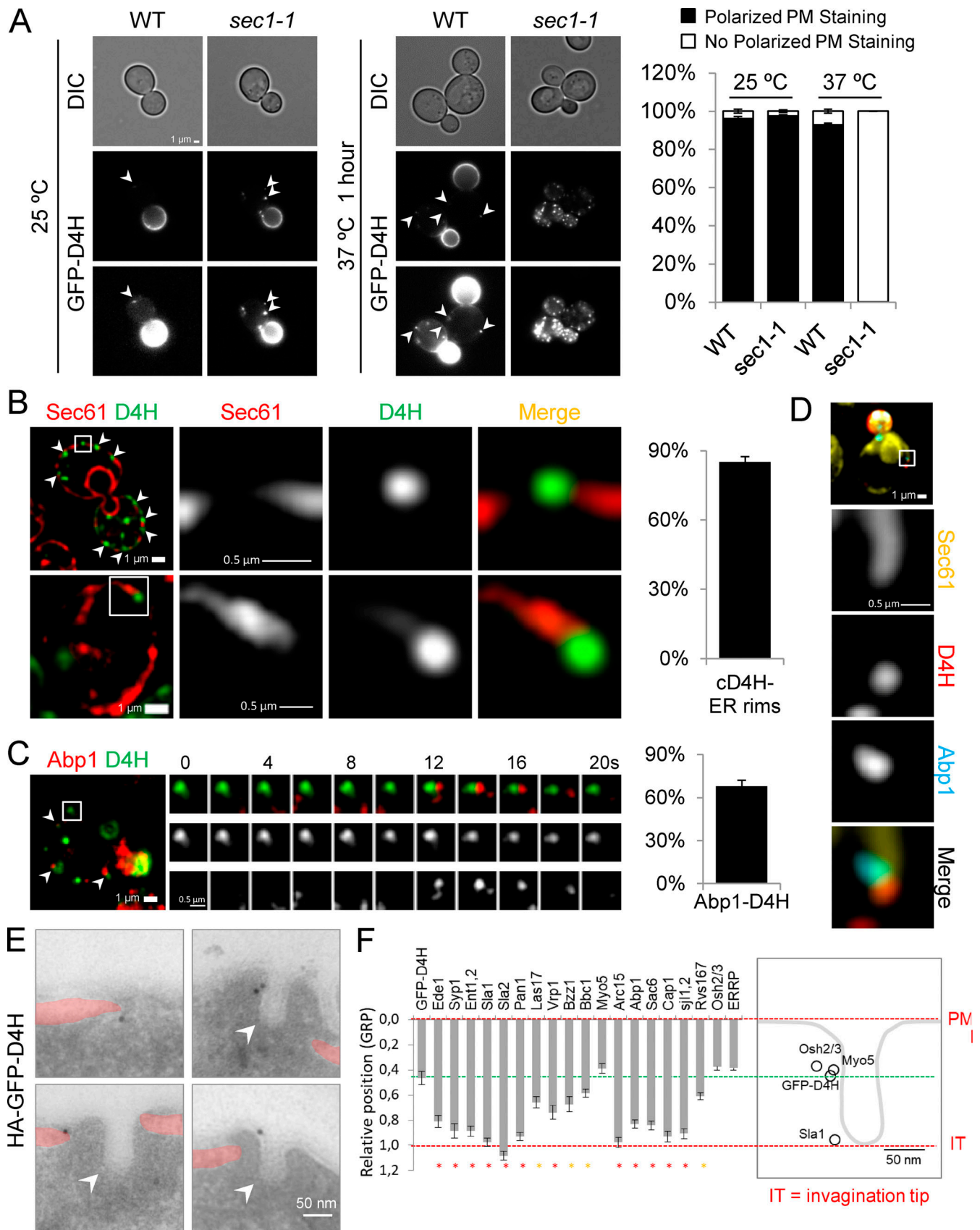


Figure 1. **Asymmetric distribution of GFP-D4H.** (A) Single-focal plane differential interference contrast (DIC) and fluorescence micrographs (FMs) of indicated strains expressing GFP-D4H, at indicated temperatures. Arrowheads point to vesicle-like structures. The same micrograph with enhanced brightness is

shown. Average  $\pm$  SEM frequencies of polarized PM staining are indicated.  $n > 100$  cells from three experiments. **(B and C)** Merged FMs of five 0.1- $\mu$ m focal planes of cells expressing GFP-D4H and either Sec61-mCherry (B) or Abp1-mCherry (C). Individual channels and merged magnified frames (B) or time lapses (C) are shown. Average  $\pm$  SEM frequencies of colocalization between cortical GFP-D4H patches and Sec61-mCherry rims (B) or Abp1-mCherry patches (C).  $n > 100$  rims or patches from three experiments. **(D)** Merged FM of a cell expressing Sec61-YFP, mCherry-D4H, and Abp1-CFP. Individual channels and merged magnified frames are shown. **(E)** Electron micrographs of a cER rim or ER-endocytic MCSs immunolabeled for HA-GFP-D4H. cER colored in red. Arrowheads point to endocytic invaginations. **(F)** QEM analysis showing colocalization of HA-GFP-D4H labeling with endocytic proteins and ER rims. Average  $\pm$  SEM for GRP of the indicated endocytic proteins or the GFP-D4H probe or the ER relative position (ERRP) are indicated. Refer to Fig. S2 A for details. Red asterisks,  $P < 0.001$ ; orange asterisks,  $0.001 \leq P < 0.1$ ; absence of asterisks,  $P > 0.1$ ;  $t$  test.  $n > 100$  gold particles/invaginations for endocytic proteins and ER rims, and  $n > 40$  for Osh2/3 and GFP-D4H gold particles/invaginations.

et al., 2018; Maekawa, 2017; Marek et al., 2020; Savinov and Heuck, 2017; Fig. S1 A) at levels that did not alter the cortical dynamics of the endocytic coat component Sla1-GFP (Fig. S1 B). Inspection of yeast expressing GFP-D4H unveiled a strong PM staining in small to medium-sized daughter cells (Fig. 1 A; Video 1 and Video 2). The strong staining persisted from bud emergence to initial phases of cytokinesis, where labeling accumulated at the bud neck (Video 1). At bud emergence, small vesicles moved toward the bud (Video 1). In addition, cortical, less-dynamic GFP-D4H patches were visible in mother cells at longer exposures (Fig. 1 A and Video 2). The probe recognized sterols, since the vesicular structures and the PM staining disappeared in *erg11* and *erg28* mutants (Fig. S1, C and D) or in yeast incubated with the Erg1 inhibitor terbinafine (TBF; Bhattacharya et al., 2018; Fig. S1, C and E). These results suggested that secretory vesicles enriched in sterols (Klemm et al., 2009) might load the PM of daughter cells. Consistently, the polarized GFP-D4H staining was lost in secretory mutants (Spang, 2015; *sec1-1*, *sec8-6*, *sec6-4*, and *sec4-8*) at restrictive temperature (Figs. 1 A and S1 F). The Golgi-localized Osh4, which contributes to polarized secretion (Alfaro et al., 2011; Antonny et al., 2018; Fang et al., 1996; Kozminski et al., 2006; Li et al., 2002; Ling et al., 2014; Smindak et al., 2017), also played a prominent role in the process, as compared with other Oshes (Fig. S1 G).

### Osh2 uses PI4P counter-transport to extract sterols from ERSEs

In mother cells, more than 85% of the cortical GFP-D4H (cGFP-D4H) patches localized at rims of the cortical ER (cER; Fig. 1 B and Video 3). The GFP-D4H patches followed the ER dynamics (Video 4) and sometimes spread toward the ER (Fig. 1 B), indicating that they were linked. More than 65% of the cGFP-D4H also associated with transient foci of Abp1-mCherry, a marker of endocytic actin (Fig. 1 C). Triple labeling further demonstrated mCherry-D4H patches at cER rims, some associated with endocytic sites (Fig. 1 D). Quantitative immunoelectron microscopy (QEM) showed specific HA-GFP-D4H labeling at cER rims and the invagination neck and base (Figs. 1 E and S2 A). Analysis of the gold relative position (GRP; Fig. S2 A) showed coincidence of the HA-GFP-D4H labeling with that of Myo5 and Osh2/3 and, to a lesser extent, with the yeast amphiphysin Rvs167 and N-WASP, Las17 (Fig. 1 F).

The data suggested that sterols were accessible at certain cER subdomains, from where they could be extracted by Osh2. Consistently, the number and brightness of cGFP-D4H patches increased in the absence of Osh2 (Fig. 2 A). QEM further demonstrated the presence of engrossed HA-GFP-D4H-labeled cER

rims in *osh2 $\Delta$*  cells (Fig. 2 B). Deletion of Osh4 also caused accumulation of GFP-D4H foci, but mostly noncortical (Fig. S2 B). In this strain, the ER was grossly altered, with very little cER (Fig. S2 B). Depletion of the endocytic Osh3, which does not extract sterols (Encinar del Dedo et al., 2017; Schulz et al., 2009; Tong et al., 2013), or depletion of the sterol transporter Osh1, which sits on the nucleus/vacuole junction (Kvam and Goldfarb, 2004; Levine and Munro, 2001) and the Golgi (Levine and Munro, 2001), had no effect on the cGFP-D4H patches (Fig. 2 A).

To directly investigate if Osh2 extracted sterols from cER rims, we followed individual cGFP-D4H patches upon addition of TBF in either the presence or absence of Osh2. The GFP intensity immediately dropped upon drug imposition in WT cells but remained unaltered in the absence of Osh2 (Figs. 2 C and S2 C). Fenpropimorph (FPM), a downstream inhibitor, had a similar effect (Fig. S1 C; and Fig. S2, C and D; Marcireau et al., 1990). Upon 1-h TBF incubation, the GFP-D4H patch intensity dropped in WT, *osh1 $\Delta$* , and *osh3 $\Delta$*  cells but was unaltered in *osh2 $\Delta$*  yeast (Fig. S2 E). Thus, the data indicated that the cGFP-D4H patches decorated Osh2-dependent ERSEs. In agreement, Osh2-YFP transiently colocalized with mCherry-D4H at cER rims (Fig. 2 D).

Interestingly, treatment with OSW-1, an inhibitor of OSBP (Mesmin et al., 2017), had the opposite effect of TBF on the cGFP-D4H patch intensity in WT cells (Fig. 2 C; and Fig. S2, C and F). Similar to TBF, the OSW-1 effect required Osh2, but not Osh1 or Osh3 (Fig. 2 C; and Fig. S2, C and F). 1-h OSW-1 treatment did not grossly alter the polarized sterol pattern (Fig. S2 G).

As expected, Osh2 function at ERSEs required its sterol transfer activity. Deletion of its ORD (OSBP-related lipid-binding domain; *osh2-ORD $\Delta$* ) increased the cGFP-D4H patch intensity, which was restored to WT levels by expression of a chimera of the Osh2 N terminus with the Osh4 ORD (*osh2-ORD4*), but not with that of Osh6 (*osh2-ORD6*; Figs. 2 E and S2 H). In addition, mutation of the “double F in an acidic track” (FFAT) motif (*osh2-FFAT\**) impaired sterol extraction, indicating that Osh2 function required binding to VAPs (Encinar del Dedo et al., 2017; Figs. 2 E and S2 H). Finally, sterol extraction relied on PI4P counter-transport. Mutation of the Osh2 H1000, H1001, and R1230, predicted to impair PI4P and phosphatidylinositol 4,5-bisphosphate (PI(4,5)P<sub>2</sub>) binding (*osh2-HHR\**; de Saint-Jean et al., 2011; Wang et al., 2019), increased the cGFP-D4H patch intensity, while mutation of the surface patch III K1114, K1116, and K1118, required to sustain ORP2 PI(4,5)P<sub>2</sub> sterol counter-transport (Wang et al., 2019), did not. Further, depletion of Osh2 and Osh3 significantly increased the PM PI4P levels in mother cells (Stefan et al., 2011; Fig. S2 I), and expression of Osh2, but not

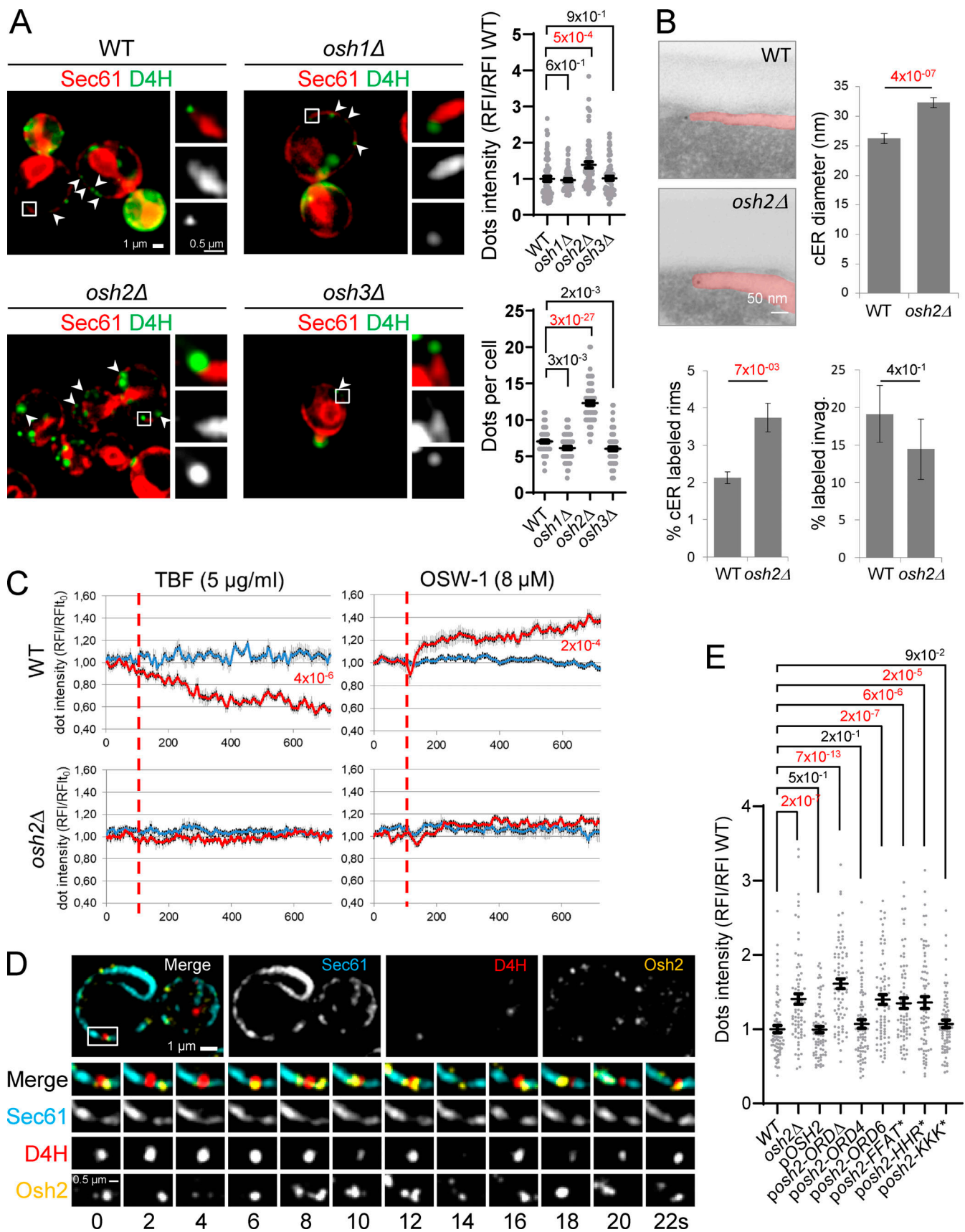


Figure 2. **Osh2 extracts sterols from cortical ERSEs.** (A) Merged FMs of the indicated strains expressing GFP-D4H and Sec61-mCherry. Arrowheads point to contacts. Individual channels and merged magnified areas are shown. Average  $\pm$  SEM and *t* test P values of the cGFP-D4H patch relative fluorescence

intensity (RFI) normalized to WT or their number per cell are indicated. Significant differences are shown in red ( $n > 210$  dots and  $n > 100$  cells, respectively). **(B)** Electron micrographs of WT or *osh2Δ* cells expressing HA-GFP-D4H, immunodecorated for the HA epitope. cER is in red. Average  $\pm$  SEM and *t* test *P* values of cER diameter and percentage of labeled ER rims or invaginations in WT and *osh2Δ* cells are indicated. Refer to Fig. S2 A for details. Significant differences are shown in red ( $n > 300$  cER rims and  $n > 80$  invaginations). **(C)** Time course of cortical GFP-D4H patch RFI, normalized to time 0, in WT or *osh2Δ* cells mock treated (blue) or treated (red) with the indicated drugs. The drug was added 2 min after initiation of the experiment (red line). *t* test *P* values showing significant differences in the last time recorded for the WT are indicated ( $n \geq 10$ ). **(D)** Merged FMs of cells expressing Sec61-CFP, mCherry-D4H, and Osh2-YFP. Individual channels and merged time lapses are shown. **(E)** Average  $\pm$  SEM and *t* test *P* values of cortical GFP-D4H patch RFI normalized to WT (*pOSH2*) in *osh2Δ* cells expressing the empty plasmid (*osh2Δ*) or plasmids encoding the indicated *OSH2* alleles. Significant differences are in red ( $n > 80$  patches).

Osh2-HHR\*, partially restored the PI4P levels in the mutant (Fig. S2 I). Instead, no significant elevation of the PM PI(4,5)P<sub>2</sub> was detected in the mutants (Fig. S2 I).

### A subset of Ergs localizes at ERSEs

Most Ergs localize throughout the ER (Dubreuil et al., 2019). However, the observation that GFP-D4H accumulated at discrete ER zones suggested that some sterol modifications recognized by the probe might occur at ERSEs. Consistently, we found that Erg7, Erg27, Erg6, and Erg2 (Fig. S1 C) showed a punctuated pattern, with bright spots near the nuclear envelope and fainter cortical patches associated to cER rims (Fig. 3 A and Video 5; Dubreuil et al., 2019). Erg7 closes the aromatic rings of the squalene epoxide, and Erg27 reduces the C3 oxygen, two molecular features recognized by PFO (Fig. S1 C; Maekawa, 2017). Consistent with a dense network of Erg contacts (Mo and Bard, 2005), double labeling demonstrated that these enzymes colocalized in all structures (Fig. S3 A and Video 6). The bright perinuclear Erg6-GFP spots, but not the fainter cortical patches, were lipid droplets (LDs) stainable with BODIPY (Fig. S3 B; Joshi et al., 2018). Reciprocally, a significant fraction of cortical Erg patches, but not LDs, associated with GFP-D4H (Fig. 3 B; and Video 7 and Video 8), labeling cortical ERSEs. In agreement, the cortical Erg patches marked endocytic hot spots (Figs. 3 C and S3 C; Video 9 and Video 10).

The data indicated that ERSEs accumulated a subset of sterol biosynthetic enzymes, which could physically contact the components of the ER-endocytic MCSs. In fact, coimmunoprecipitation (Fig. 3 D) and two-hybrid assays (Fig. 3 E) detected interactions between Myo5 and Erg6 or Erg27. The Erg-binding region in Myo5 included the TH2 (tail homology 2) domain and did not overlap with that for Osh2 (Encinar del Dedo et al., 2017), indicating a role for myosin-I as a scaffold, holding the sterol biosynthetic and transport machineries (Fig. 3 F). In addition, we demonstrated binding of Erg6 with the ORD of Osh2 in immunoprecipitation (Fig. 3 D; and Fig. S3, D and E), two-hybrid (Fig. 3 G), and pull-down assays (Fig. S3 F). Again, the Osh2-binding sites for Erg6 and Myo5 did not overlap (Fig. 3 G; Encinar del Dedo et al., 2017). Fluorescence microscopy also showed contact between the sterol synthesis and transport machineries (Fig. 3 H). No interaction between Erg6 and other Oshes was detected in two-hybrid assays, nor could we find binding between Osh4 and Erg2, Erg6, Erg7, or Erg27 in immunoprecipitations (Figs. 3 G and S3 E), suggesting that Osh2 plays a prominent role at cortical ERSEs. This did not discard specialized ER subdomains serving lipids to other transporters. This is likely for Osh4, which interacts with Erg11 (Tarassov et al., 2008) and whose depletion results in the accumulation of GFP-D4H foci (Fig. S2 B).

To test the functional significance of the Erg-Osh2 interaction, we mutated the PPPVP motif that mediates binding of Osh2 to Myo5 (Encinar del Dedo et al., 2017) within the *osh2-ORD4* chimera, to generate a mutant *osh2-ORD4-PPPVP\** unable to directly or indirectly interact with the Ergs at ERSEs (Fig. 3, E–G). *Osh2-ORD4-PPPVP\** failed to restore sterol extraction in an *osh2Δ* background (Fig. 3 I). Further sustaining the functional relevance of the Erg/Osh interaction, a chimera of Erg6 and Osh4 reduced the brightness of the cGFP-D4H patches to WT levels in *osh2Δ* cells, whereas neither of the two proteins did when separately expressed (Fig. 3 I). Also consistent with a key nonenzymatic scaffolding role of Erg6 sustaining sterol extraction was the observation that a catalytically inactive Erg6 (*erg6-D152L*) restored growth and sterol extraction in an *erg6Δ* strain, similar to the WT (Nes et al., 2004; Fig. 3, J and K).

### Asymmetric control of sterol-dependent endocytosis in yeast

Even though sterols are essential for endocytosis in yeast (Encinar del Dedo et al., 2017; Munn et al., 1999), our work showed that the sterol transport routes markedly differ in mother and daughter cells. Thus, we hypothesized that the mechanisms supporting endocytosis might diverge. PM accessible sterols in mothers are kept low, perhaps to prevent ectopic activation of the PI4P5 kinase (Nishimura et al., 2019) or assembly of the Exocyst (Inoue et al., 2006). This might impose the need for a localized sterol transport to endocytic sites. In daughters, loaded with sterols in a secretory pathway-dependent manner (Fig. 1 A), on-site sterol transfer should be dispensable. Consistent with this view, treatment of yeast with FPM and OSW-1 immediately delayed and weakened actin polymerization at endocytic sites in mother cells and consequently extended the life span of Sla1-GFP (Fig. 4, A and B). However, endocytosis in daughters smaller than 2  $\mu$ m in diameter, essentially devoid of ERSEs, was unaltered under these experimental conditions (Fig. 4 A). This was despite sterols being equally required for endocytosis, as demonstrated by acute sterol sequestration with filipin or prolonged FPM and OSW-1 treatments (Fig. 4 A), which completely altered the sterol homeostasis (Fig. S3 G).

Also in agreement with the diverse sterol routes, depletion of Osh2 significantly expanded the life span of Sla1 in mothers (Fig. 5 A), but not in daughters (Fig. 5 A). The capacity of *osh2* alleles to sustain endocytosis correlated with their capacity to extract sterols (Fig. S3 H; Encinar del Dedo et al., 2017). Reciprocally, preventing secretion, strongly influenced endocytic uptake in daughter cells (Johansen et al., 2016; Riezman, 1985), but not in mothers (Fig. 5 B).

Further sustaining a universal requirement for sterols in endocytosis, depletion of Erg28, cofactor of the essential Erg27,

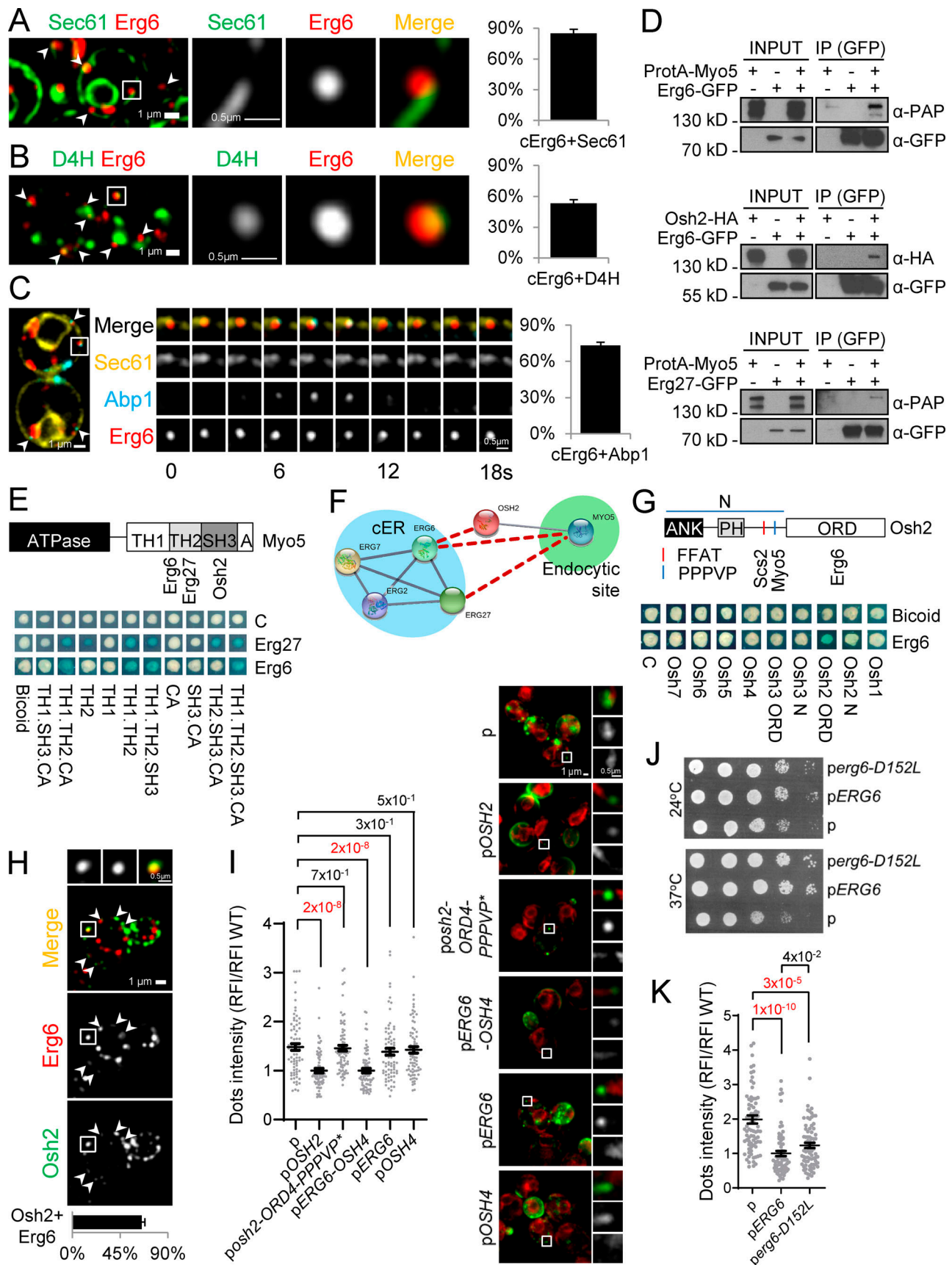


Figure 3. **A subset of Ergs accumulates at ERSESS.** (A and B) Merged FMs of cells expressing Erg6-mCherry and Sec61-GFP (A) or GFP-D4H (B). Individual channels and merged magnified areas are shown. Average  $\pm$  SEM frequencies of colocalization of cortical Erg6-mCherry with Sec61-GFP (A) or GFP-D4H (B) are

indicated.  $n > 75$  rims or patches. **(C)** Confocal FMs of cells expressing Sec61-YFP, Abp1-CFP, and Erg6-mCherry. Individual channels and merged magnified time lapses are shown. Arrowheads point to contacts. Average  $\pm$  SEM frequencies of colocalization of Erg6-mCherry with Abp1-CFP are indicated.  $n > 100$  from three experiments. **(D)** Immunoblots of anti-GFP agarose precipitates (IP [GFP]) from yeast expressing protein A (ProtA), GFP, and/or HA-tagged proteins (+) or nontagged (-), probed for the indicated epitopes. 10  $\mu$ g of total protein was loaded as input. **(E and G)** Diagram of interactions and two-hybrid assays of Ergs versus Myo5 (E) or Oshes (G). Blue indicates interaction. BICOID was used as negative control. TH1, tail homology 1; SH3, Src homology 3; CA, central and acidic; ANK, ankyrin repeats; PH, Pleckstrin homology; N, N-terminal domain. **(F)** Protein-protein interaction network. The purple lines are reported interactions (Encinar del Dedo et al., 2017; Mo and Bard, 2005). Red lines are described here. **(H)** Individual channels and merged FMs of cells expressing Erg6-mCherry and Osh2-GFP. Individual channels and merged magnified insets are shown. Average  $\pm$  SEM frequencies of colocalization of cortical Erg6-mCherry with Osh2-GFP indicated.  $n > 125$  from three experiments. **(I)** Average  $\pm$  SEM and  $t$  test  $P$  values of cortical GFP-D4H patch RFI normalized to WT (*pOSH2*) in *osh2 $\Delta$*  cells expressing the empty plasmid or plasmids encoding *OSH2* alleles. Significant differences are red ( $n > 210$ ). Merged FMs of the corresponding cells and merged and individual channels of magnified areas shown. **(J)** Serial dilutions of *erg6 $\Delta$*  cells bearing an empty plasmid (p) or plasmids encoding the WT *ERG6* or a catalytically inactive mutant (*erg6-D152L*) grown at the indicated temperatures. **(K)** GFP-D4H cortical patch RFI normalized to the WT (*pERG6*) for *erg6 $\Delta$*  cells bearing an empty plasmid (p) or plasmids encoding *ERG6* or *erg6-D152L*.

affected endocytic uptake in mother and daughter cells, similar to filipin (Fig. 5 C). In contrast, depletion of Erg6, which played a catalytically independent role at ERSEs (Fig. 3, J and K), affected endocytic uptake only in mothers (Fig. 5 C). Finally, deletion of the Myo5 TH2 domain, which mediated binding to Erg6 and Erg27 (Fig. 3 E), sensitized mother cells, but not daughter cells, to very low concentrations of filipin (Fig. 5 D). Altogether, the data demonstrated that on-site coupling of the sterol synthesis and transport machineries was required to sustain endocytosis in mother cells, but not in daughters, where PM loading with accessible sterols and endocytosis were linked to secretion.

## Materials and methods

### Strains and growth conditions

The yeast strains used in this study are listed in Table 1. GFP, mCherry, YFP, and HA tags were fused at the C terminus of each protein by homologous recombination in the genome as described previously (Wach et al., 1997) using 50-nt oligonucleotides upstream and downstream of the stop codon. Genome-edited strains behaved as WT. Strains without plasmids were grown in complete yeast peptone dextrose and strains with plasmids were selected on synthetic dextrose complete (SDC) lacking the appropriate nutrient (Dulic et al., 1991) at 25°C. Transformation of yeast was accomplished by the lithium acetate method (Ito et al., 1983). Strains used in this work are listed below.

### DNA techniques and plasmid construction

DNA manipulations were performed as described previously (Sambrook et al., 1989). Enzymes for molecular biology were obtained from New England Biolabs. PCRs were performed with a Vent polymerase (New England Biolabs) and a TRIO thermo-block (Biometra). All plasmids used in this study bear ampicillin resistance for selection in *Escherichia coli* and are listed in Table 2, where the yeast features and inserts are described. The *osh2-HHR\** ORF was synthesized by Genescript. Information about the construction strategies are available upon request. The oligonucleotides used in this work for plasmid construction are listed below (Table 3).

### SDS-PAGE, immunoblots, and antibodies

SDS-PAGE was performed as described previously (Laemmli, 1970) using precasted Mini-PROTEAN TGX 4–20% acrylamide

gels (Bio-Rad). For immunoblot, nitrocellulose membranes (Protran BA85; GE Healthcare) were probed with anti-HA (Anti-HA-Peroxidase High Affinity 3F10; Roche), peroxidase anti-peroxidase (Sigma-Aldrich) or anti-GFP (monoclonal antibody JL-8; Living Colors), followed by a peroxidase-conjugated secondary goat anti-rabbit IgG antibody (Sigma-Aldrich). Protein transfer, blotting, and chemiluminescence detection were performed using standard procedures. Detection of proteins was performed using the ECL kit (GE Healthcare).

### Subcellular fractionation and immunoprecipitations

For the anti-GFP-agarose immunoprecipitations from P13000 extracts, cells were glass bead-lysed in LB (25 mM Tris and 5 mM EDTA, pH 8.5) in the presence of protease inhibitors (1 mM PMSF, 5  $\mu$ g/ml Leupeptine, 2.5  $\mu$ g/ml Antipain, 1  $\mu$ g/ml Pepstatin, and 1  $\mu$ g/ml Aprotinin). Unbroken cells were eliminated at 700  $g$  for 15 min at 4°C. The supernatant was diluted with the same volume of BB (10 mM Tris, 0.2 mM EDTA, and 0.2 mM DTT, pH 7.5) containing protease inhibitors. The post-700  $g$  supernatants were spun at 13,000  $g$  for 20 min, and the pellet was recovered and resuspended in 1 ml IP buffer (50 mM Tris, 150 mM NaCl, 5 mM EDTA, and 1% Triton X-100, pH 7.5). The extract was adjusted to 1 mg protein per ml, incubated 30 min at 4°C, and spin at 700  $g$  for 15 min. The supernatant was incubated with 20  $\mu$ l of 50% anti-GFP-Agarose (GFP-trap; Chromotek) for 1 h at 4°C. Beads were washed with IP buffer and subsequently with IP buffer without Triton X-100 and boiled in 25  $\mu$ l SDS-PAGE sample buffer.

### Two-hybrid assays

The Interaction Trap two-hybrid system was used (Gyuris et al., 1993). Plasmids pEG202, pJG4-5, and pSH18-34 and the strain EGY48 were kindly provided by Dr. R. Brent (Fred Hutchinson Cancer Research Center, Seattle, WA). To measure  $\beta$ -galactosidase activity, EGY48 cells bearing the *lexAop-lacZ* reporter plasmid pSH18-34 were cotransformed with the appropriate pEG202- and pJG4-5-derived plasmids and streaked out on 5-bromo-4-chloro-3-indolyl- $\beta$ -D-galactopyranoside containing Synthetic Dextrose/Gal/Raf-His-Trp-Ura plates (0.67% yeast nitrogen base [Difco], 7 g/liter  $\text{Na}_2\text{HPO}_4$ , 3 g/liter  $\text{NaH}_2\text{PO}_4$ , 2% galactose, 1% raffinose, 40 mg/ml leucine, 80 mg/liter 5-bromo-4-chloro-3-indolyl- $\beta$ -D-galactopyranoside [Sigma Chemicals], and 2% agar, pH 7). Pictures were taken after 2 d of growth at 24°C.

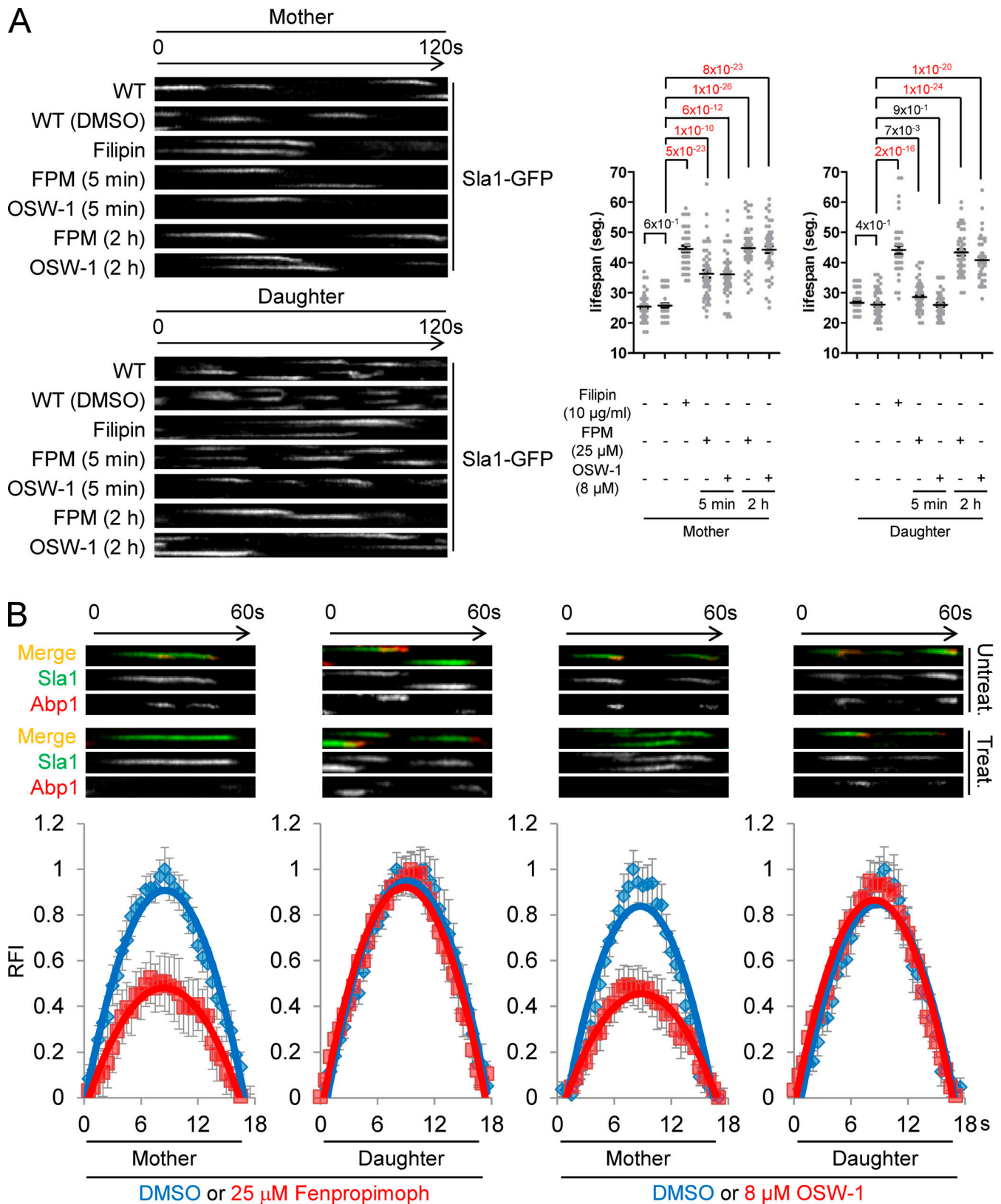


Figure 4. **Asymmetric regulation of sterol-dependent endocytosis in yeast.** (A) Average  $\pm$  SEM life span and *t* test *P* values of Sla1-GFP cortical patches in mother and daughter cells of WT cells mock treated (DMSO, +) or treated with the indicated drugs, concentrations, and times. Significant differences are shown in red ( $n > 150$ ). Kymographs of time-lapse fluorescence movies of cortical Sla1-GFP patches for each experimental condition shown. Images were taken every 0.5 s. (B) Merged kymographs of cortical patches (upper panels) of time-lapse fluorescence movies of cells expressing Sla1-GFP and Abp1-mCherry, mock treated (DMSO) or treated 5 min with FPM or OSW-1. Images taken every 0.5 s. Average  $\pm$  SEM of cortical Abp1-mCherry patch RFI in mock-treated cells (blue) or under the indicated treatments (red;  $n > 60$ ).



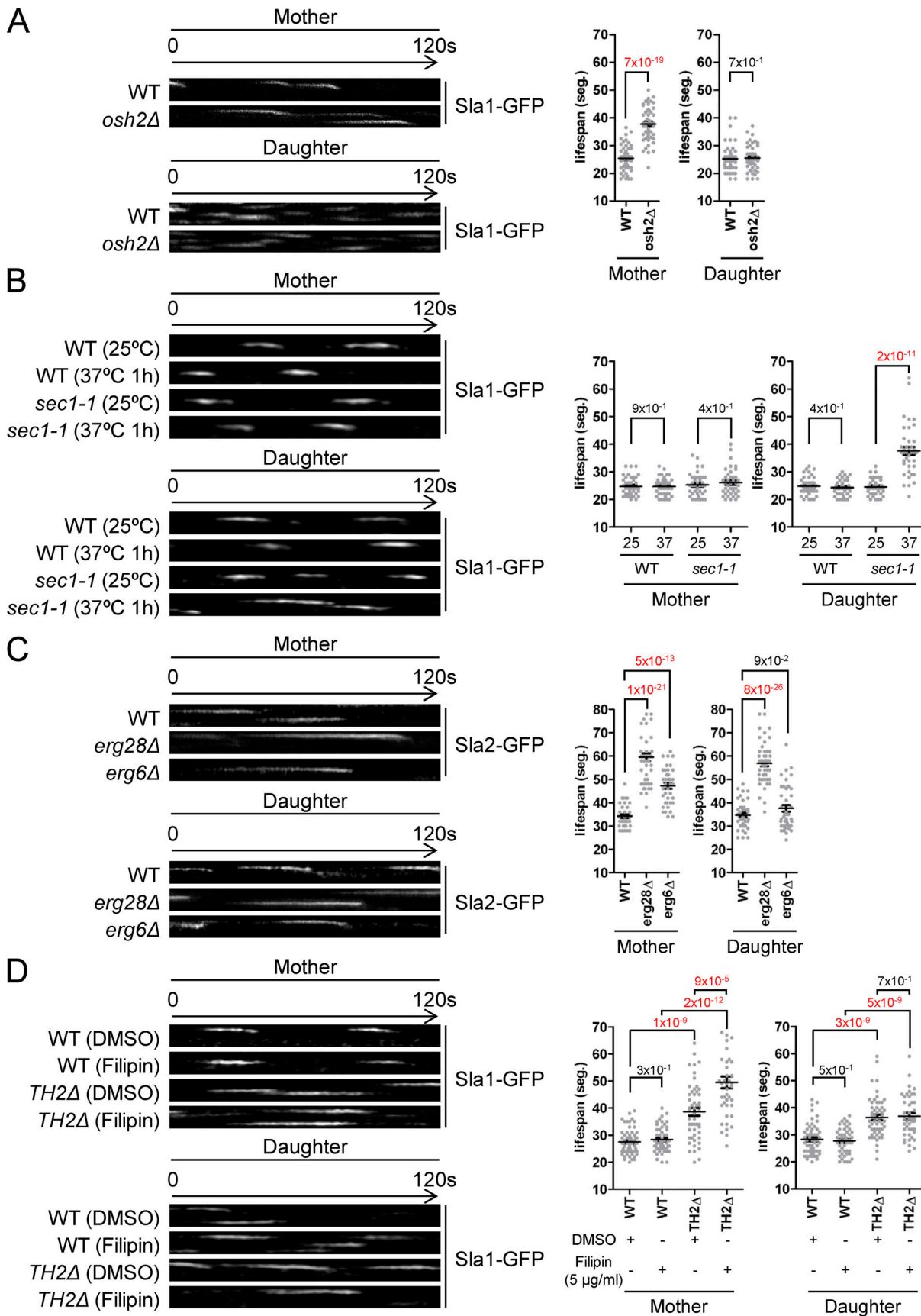


Figure 5. **Localized sterol transfer is required for endocytic uptake only in mother cells.** (A–D) Average  $\pm$  SEM life span and *t* test P values of Sla1-GFP (A, B, and D) or Sla2-GFP (C) cortical patches in mother and daughter cells of WT cells or the indicated mutants, untreated, mock treated (DMSO, +), or treated with filipin (D). Significant differences are shown in red ( $n > 150$ ). Kymographs of time-lapse fluorescence movies of cortical Sla1-GFP patches for each experimental condition are shown. Images were taken every 0.5 s.

Table 1. **Strains used in this work**

Strain	Genotype	Reference
SCMIG381	<i>Mata his3 leu2 met15 ura3</i>	Euroscarf
SCMIG1527	<i>Mata his3 leu2 met15 ura3 erg28Δ::KMX</i>	Euroscarf
SCMIG1549	<i>Mata his3 leu2 met15 ura3 erg6Δ::KMX</i>	Euroscarf
SCMIG1550	<i>Mata his3 leu2 met15 ura3 erg11-td::KMX</i>	Euroscarf
SCMIG372	<i>Mata his3 leu2 met15 ura3 osh1Δ::KMX</i>	Euroscarf
SCMIG373	<i>Mata his3 leu2 met15 ura3 osh2Δ::KMX</i>	Euroscarf
SCMIG374	<i>Mata his3 leu2 met15 ura3 osh3Δ::KMX</i>	Euroscarf
SCMIG375	<i>Mata his3 leu2 met15 ura3 osh4Δ::KMX</i>	Euroscarf
SCMIG376	<i>Mata his3 leu2 met15 ura3 osh5Δ::KMX</i>	Euroscarf
SCMIG558	<i>Mata his3 leu2 met15 ura3 osh6Δ::KMX</i>	Euroscarf
SCMIG537	<i>Mata his3 leu2 met15 ura3 osh7Δ::KMX</i>	Euroscarf
SCMIG1498	<i>Mata his3 leu2 met15 ura3 osh2Δ::KMX osh3Δ::KMX</i>	(Encinar del Dedo et al., 2017)
SCMIG1528	<i>Mata his3 leu2 met15 ura3 sec1-1::KMX</i>	O. Gallego (UPF, Barcelona Spain)
SCMIG1529	<i>Mata his3 leu2 met15 ura3 sec8-6::KMX</i>	O. Gallego (UPF, Barcelona Spain)
SCMIG1530	<i>Mata his3 leu2 met15 ura3 sec6-4::KMX</i>	O. Gallego (UPF, Barcelona Spain)
SCMIG1531	<i>Mata his3 leu2 met15 ura3 sec4-8::KMX</i>	C. Roncero (IBFG, Salamanca, Spain)
SCMIG1519	<i>Mata his3 leu2 trp1 ura3 bar1 SEC61-mCherry::HISMX</i>	Encinar del Dedo et al., 2017
SCMIG1548	<i>Mata ura3 leu2 his3 met15 osh1Δ::KMX SEC61-mCherry::HISMX</i>	This study
SCMIG1521	<i>Mata ura3 leu2 his3 met15 osh2Δ::KMX SEC61-mCherry::HISMX</i>	Encinar del Dedo et al., 2017
SCMIG1546	<i>Mata ura3 leu2 his3 met15 osh3Δ::KMX SEC61-mCherry::HISMX</i>	This study
SCMIG1547	<i>Mata ura3 leu2 his3 met15 osh4Δ::KMX SEC61-mCherry::HISMX</i>	This study
SCMIG1141	<i>Mata his3 leu2 trp1 ura3 bar1 SLA1-mCherry::HISMX</i>	This study
SCMIG1532	<i>Mata his3 leu2 met15 ura3 ERG6-mCherry::HISMX</i>	This study
SCMIG1533	<i>Mata his3 leu2 met15 ura3 ERG6-mCherry::HISMX Erg7-LII-GFP::KMX</i>	This study
SCMIG1534	<i>Mata his3 leu2 met15 ura3 ERG6-mCherry::HISMX Erg27-GFP::KMX</i>	This study
SCMIG1535	<i>Mata his3 leu2 ura3 ERG6-mCherry::HISMX Erg2-LII-GFP::HISMX</i>	This study
SCMIG1536	<i>Mata his3 leu2 ura3 ERG6-mCherry::HISMX Sec61-YFP::HISMX</i>	This study
SCMIG1537	<i>Mata his3 leu2 met15 ura3 ERG27-GFP::HISMX</i>	This study
SCMIG1538	<i>Mata his3 leu2 met15 ura3 ERG6-GFP::HISMX</i>	This study
SCMIG1539	<i>Mata his3 leu2 met15 ura3 ERG6-GFP::HISMX Scs2-HA::KMX</i>	This study
SCMIG1540	<i>Mata his3 leu2 met15 ura3 ERG2-LII-GFP::HISMX</i>	This study
SCMIG1541	<i>Mata his3 leu2 trp1 ura3 bar1 ERG7-LII-GFP::TRPMX</i>	This study
SCMIG1542	<i>Mata his3 leu2 met15 ura3 ERG27-GFP::HISMX Scs2-HA::KMX</i>	This study
SCMIG1543	<i>Mata his3 leu2 lys2 ura3 ERG7-LII-GFP::HISMX Scs2-HA::KMX</i>	This study
SCMIG1544	<i>Mata his3 leu2 met15 ura3 erg6Δ::KMX</i>	Euroscarf
SCMIG277	<i>Mata ade2 his3 myo3Δ::HIS3 mycMYO5::URA3::myo5Δ::TRP1 leu2 trp1 ura3 bar1</i>	Geli et al, 2000
SCMIG278	<i>Mata his3 myo3Δ::HIS3 mycmyo5-TH2nΔ::URA3::myo5Δ::TRP1 leu2 trp1 ura3 bar1</i>	Geli et al, 2000
SCMIG1495	<i>Mata his3 leu2 met15 ura3 SLA1-GFP::HISMX</i>	Encinar del Dedo et al., 2017

### Fluorescence microscopy

Unless otherwise stated, samples were observed on a Leica DMI6000 wide-field microscope equipped with a 63× APO (Apochromatic; NA 1.4) oil-immersion objective, a Hamamatsu Orca-R2 camera and a SOLA-SMII white LED illumination source. A fast external filter wheel for GFP (BP470/40) and

mCherry (BP572/35) excitation was used to minimize channel acquisition mismatch. The system was controlled under the LAS X (Leica Application Suite X) software. Cells were grown to mid-log phase, harvested, diluted in a small volume of SDC medium, and imaged as wet mounts on a 2% agarose patch on the same medium and at the same temperature used for culture

Table 2. **Plasmids used in this work**

<b>Plasmids</b>	<b>Yeast features</b>	<b>Insert</b>	<b>Reference</b>
pRS316GFP-D4H	CEN4 URA3	GFP-PFO-D4-D434S	<a href="#">Koselny et al., 2018</a>
pRS316GFP-D4H <i>ura3Δ::LEU2</i>	CEN4 LEU2	GFP-PFO-D4-D434S	This study
pRS316HA-GFP-D4H	CEN4 URA3	3HA-GFP-PFO-D4-D434S	This study
p111SLA2-GFP	CEN4 LEU2 HIS5	SLA2-GFP	This study
p33ABP1-mCherry	CEN4 URA3 HIS3	ABP1-mCherry	<a href="#">Encinar del Dedo et al., 2017</a>
p33ABP1-mCherry. <i>ura3Δ::LEU2</i>	CEN4 LEU2 HIS3	ABP1-mCherry	<a href="#">Encinar del Dedo et al., 2017</a>
p33PA-MYO5	CEN4 URA3	ProteinA-MYO5	<a href="#">Grosshans et al., 2006</a>
p33MYO5	CEN4 URA3	MYO5	<a href="#">Geli and Riezman, 1996</a>
pLexA-MYO5-tail	2μ HIS3	LexA- <i>myo5</i> (aa 757–1,219)	<a href="#">Geli et al., 2000</a>
pLexA-MYO5-TH2.SH3.CA	2μ HIS3	LexA- <i>myo5</i> (aa 984–1,219)	<a href="#">Grötsch et al., 2010</a>
pLexA-MYO5-SH3.CA	2μ HIS3	LexA- <i>myo5</i> (aa 1,085–1,219)	<a href="#">Grötsch et al., 2010</a>
pLexA-MYO5-CA	2μ HIS3	LexA- <i>myo5</i> (aa 1,142–1,219)	<a href="#">Grötsch et al., 2010</a>
pLexA-MYO5-TH1.TH2.SH3	2μ HIS3	LexA- <i>myo5</i> (aa 757–1,181)	<a href="#">Grötsch et al., 2010</a>
pLexA-MYO5-TH1.TH2	2μ HIS3	LexA- <i>myo5</i> (aa 757–1,091)	<a href="#">Grötsch et al., 2010</a>
pLexA-MYO5-TH1	2μ HIS3	LexA- <i>myo5</i> (aa 757–996)	<a href="#">Grötsch et al., 2010</a>
pLexA-MYO5-TH2	2μ HIS3	LexA- <i>myo5</i> (aa 984–1,091)	<a href="#">Grötsch et al., 2010</a>
pLexA-MYO5-SH3	2μ HIS3	LexA- <i>myo5</i> (aa 1,085–1,181)	<a href="#">Grötsch et al., 2010</a>
pLexA-BCD1	2μ HIS3	LexA-BCD1	<a href="#">Gyuris et al., 1993</a>
pLexA-ERG6	2μ HIS3	LexA-ERG6	This study
pB42-ERG6	2μ TRP1	B42-HA-ERG6	This study
pB42-ERG27	2μ TRP1	B42-HA-ERG27	This study
pJG4-5	2μ TRP1	B42-HA	<a href="#">Gyuris et al., 1993</a>
pB42-OSH1	2μ TRP1	B42-OSH1	This study
pB42-OSH2-N	2μ TRP1	B42- <i>osh2</i> (aa 1–860)	<a href="#">Encinar del Dedo et al., 2017</a>
pB42-OSH2-ORD	2μ TRP1	B42- <i>osh2</i> (aa 840–1,240)	<a href="#">Encinar del Dedo et al., 2017</a>
pB42-OSH3-N	2μ TRP1	B42- <i>osh2</i> (aa 1–604)	<a href="#">Encinar del Dedo et al., 2017</a>
pB42-OSH3ORD	2μ TRP1	B42- <i>osh2</i> (aa 605–997)	This study
pB42-OSH4	2μ TRP1	B42-OSH4	This study
pB42-OSH5	2μ TRP1	B42-OSH5	This study
pB42-OSH6	2μ TRP1	B42-OSH6	This study
pB42-OSH7	2μ TRP1	B42-OSH7	This study
Ycplac111	CEN4 LEU2	—	<a href="#">Gietz and Sugino, 1988</a>
Ycplac33	CEN4 URA3	—	<a href="#">Gietz and Sugino, 1988</a>
Ycp50	CEN4 URA3	—	<a href="#">Gietz and Sugino, 1988</a>
p111OSH2-HA	CEN4 LEU2 HIS3	OSH2-HA	<a href="#">Encinar del Dedo et al., 2017</a>
p111osh2-ORDΔ-HA	CEN4 LEU2 HIS3	<i>osh2</i> -ORDΔ-HA	<a href="#">Encinar del Dedo et al., 2017</a>
p111osh2-ORD4-HA	CEN4 LEU2 HIS3	OSH2-ORD4-HA	<a href="#">Encinar del Dedo et al., 2017</a>
p111osh2-ORD6-HA	CEN4 LEU2 HIS3	OSH2-ORD6-HA	<a href="#">Encinar del Dedo et al., 2017</a>
p111osh2-FFAT*-HA	CEN4 LEU2 HIS3	<i>osh2</i> -FYD-AAA-HA	<a href="#">Encinar del Dedo et al., 2017</a>
p111osh2-HHR*-HA	CEN4 LEU2 HIS3	<i>osh2</i> -HHR-AAA-HA	This study
p111osh2-KKK*-HA	CEN4 LEU2 HIS3	<i>osh2</i> -KKK-AAA-HA	This study
p111osh2-PPPVP*-ORD4-HA	CEN4 LEU2 HIS3	<i>osh2</i> -PPPVP-AAAA.ORD4-HA	This study
p33ERG6	CEN4 URA3	ERG6	This study
p33ERG6-OSH4-HA	CEN4 URA3 HIS3	ERG6-OSH4-HA	This study

Table 2. **Plasmids used in this work (Continued)**

Plasmids	Yeast features	Insert	Reference
pRS316OSH4-HA	CEN4 URA3 HIS3	OSH4-HA	This study
p111ERG6	CEN4 LEU2	ERG6	This study
p111erg6-D152L	CEN4 LEU2	erg6-D152L	This study
p111OSH2-YFP	CEN4 LEU2 HIS3	OSH2-YFP	Encinar del Dedo et al., 2017
pGST-ORD2	—	ORD OSH2 (aa 683–1,283)	This study

growth. For time lapses longer than 5 min, cells were mounted on slides with agarose pads prepared by dissolving 2% agarose in SDC medium containing appropriate nutrients.

Confocal live imaging was performed in an LSM Zeiss780 system equipped with a 63× APO (NA = 1.4) oil immersion objective. Two-channel time-lapse movies were acquired at 2-s intervals by line sequential scanning. Pixel size was set to 60 nm, and pinhole aperture was kept close to 1 a.u. to avoid resolution loss. Photon counting mode detection allowed to drastically reducing the amount excitation laser power, thus minimizing photobleaching and phototoxicity. GFP and mCherry conjugates were excited at 488-nm and 594-nm laser lines and registered at detection windows of 489–549 nm and 597–696 nm, respectively. For three-channel live acquisitions, the YFP was excited at 514 nm and detected at 517–553 nm, and the CFP conjugate was excited at 458 nm and detected at 463–509 nm. GFP-D4H dynamics assays were performed in a Leica Thunder 3D live cell, equipped with a 63× water immersion lens (NA 1.2), a fast and sensitive sCMOS camera DFC9000 and a Spectra-X Light Engine. GFP was excited/detected using BP475/28 and BP510/40 filters. Algorithm-driven high-speed autofocus was used to keep the cells in focus before and after addition of the drug. Built-in instant computational clearing algorithms were applied to remove out-of-focus light and allow for accurate fluorescence intensity quantification. Instant computational clearing algorithm parameters were always adjusted according to the objective used to avoid unwanted changes in object intensity or shape. Cells expressing GFP-D4H were grown to mid-log phase in SDC lacking the appropriate nutrient, harvested, diluted in a small volume of SDC medium, and placed in a 35-mm glass-bottom dish with 20-mm micro-well (ref. D35-20-1.5-N; Cellvis) previously coated with 15  $\mu$ l of 0.2 mg/ml concanavalin A (ref. C7275; Sigma-Aldrich). For the 12-min dynamics, cells were imaged in the Leica Thunder 3D, at 5 s temporal resolution for two minutes, then they were treated with the properly drug (25  $\mu$ M FPM [36772; Sigma-Aldrich], 5  $\mu$ g/ml TBF [T8826; Sigma-Aldrich], or 8  $\mu$ M OSW-1 [B0005-092456; BOC Sciences]), and the time lapse continued for 10 min. Kymographs of the cortical dots were performed and analyzed with ImageJ. For steady analysis of GFP-D4H cortical patches, only patches in touch with the PM in mother cells were considered. For analysis of endocytosis, *SLA1* was genome edited to express C-terminal GFP in the corresponding WT or mutant strains, except for *erg* mutants, where we failed to integrate the GFP tag in the genome. In this case, *Sla2*-GFP expressed from a centromeric plasmid

was used instead of *Sla1*-GFP, because it generates less cytosolic background. Cells were imaged every 0.5 s, and kymographs were generated and analyzed by ImageJ. To inspect the kinetics of endocytic proteins in daughter cells, we only considered daughter cells smaller than 2  $\mu$ m of diameter, where *Erg6*-labeled cortical ERSEs are essentially not detectable.

### QEM

Immunolectron microscopy was performed as described previously (Idrissi et al., 2008). Briefly, cells were grown in yeast extract peptone dextrose medium (to 4–5  $\times$  10<sup>6</sup> cells/ml) and harvested over a disposable Stericup 0.22- $\mu$ m-filter unit, leaving 5 ml of media. 25 ml of 1.2× fixative solution was immediately added to obtain final concentrations of 0.04 M KPO<sub>4</sub>, pH 6.6, 0.6 M sorbitol, 4% formaldehyde (Polysciences), 0.4% glutaraldehyde (Fluka), 1 mM MgCl<sub>2</sub>, 0.5 mM EGTA, 10 mM NaF, and 10 mM NaN<sub>3</sub>. Cells were then transferred to a 50-ml Falcon, and fixation was continued overnight at 4°C with rolling. Subsequent steps (metaperiodate and ammonium chloride treatments, dehydration, infiltration, embedding, and sectioning) were performed as described previously (Mulholland et al., 1994) without further modifications. For immunolabeling, ultrathin sections were incubated for 15 min in blocking buffer (10 mM KPO<sub>4</sub>, pH 7.5, 150 mM NaCl, 2% BSA, and 0.05% Tween-20), transferred to a 25- $\mu$ l drop of primary antibody in blocking buffer for 3 h, and washed over 30 min in washing buffer (10 mM KPO<sub>4</sub> buffer, pH 7.5, 150 mM NaCl, and 0.05% Tween-20). After blocking for 15 min, grids were incubated with the corresponding gold-conjugated secondary antibody for 60 min and washed first for 30 min in washing buffer and 30 min in washing buffer without Tween-20. All steps were performed at room temperature. Grids were then washed in double distilled water, fixed for 20 min in 8% glutaraldehyde, and poststained with uranyl acetate (2% in water) over 30 min and lead citrate for 30 s. Anti-HA rat monoclonal antibody (3F10; Roche) was used as primary antibodies. 12 nm gold-conjugated goat anti-rat IgG (Jackson ImmunoResearch Laboratories) was used as a secondary antibody (diluted 1:25). Ultrathin sections were examined using a Jeol 1010 transmission electron microscope at 50 kV accelerating voltage. Micrographs of the yeast PM invaginations were acquired at 100,000× magnification with a MegaView III CCD camera and the image acquisition software analySIS (Soft Imaging System). Adjustments of image size, brightness, and contrast were performed on ImageJ. Labeling was considered specific when the labeling for a specific cellular structure (ER rims or invaginations) was at least three times higher for the

Table 3. **Oligonucleotides used in this study for plasmid construction**

<b>Plasmids made in this study</b>	<b>Oligonucleotides</b>
pLexA- <i>ERG6</i>	Erg6.1D.EcoRI.TH
	AACCAACCGAATTCATGAGTGAAACAGAATTGAGAAAAAGAC
	Erg6.1152U.XhoI.TH
pB42- <i>ERG6</i>	AACCAACCTCGAGTTATTGAGTTGCTTCTTGGGAAGTTTGG
	Erg6.1D.EcoRI.TH
	AACCAACCGAATTCATGAGTGAAACAGAATTGAGAAAAAGAC
pB42- <i>ERG27</i>	Erg6.1152U.XhoI.TH
	AACCAACCTCGAGTTATTGAGTTGCTTCTTGGGAAGTTTGG
	Erg27.1D.EcoRI
pB42- <i>OSH1</i>	AACCAACCGAATTCATGAACAGGAAAGTAGCTATCGTAAC
	Erg27.1043U.SalI
	AACCAACCTCGACTTAAATGGGGTTCTAGTTTCAACAATTTG
pB42- <i>OSH3ORD</i>	OSH1.1D.EcoRI
	AACCAAGAATTCATGTCTTCGTGCTCTCTGCA
	OSH1.2580U.XhoI
pB42- <i>OSH2ORD</i>	AACCAACTCGAGTTAGAAAATATCAGCACAATCTTTAAAG
	OSH3.1813D.MfeI
	AACCAACAATTGAGCGCCAATCCTCAAC
pB42- <i>OSH4</i>	OSH3.2991U.XhoI
	AACCAACTCGAGTCACCAGAGTTGAGAAATATCAGAC
	OSH2.2518D.EcoRI
pB42- <i>OSH5</i>	AACCAAGAATTCGTGCAAAAAGAAAAGAAGAATATTAC
	OSH2.3840U.XhoI
	AACCAACTCGAGTTAAAAATGTACCACAATCTTTC
pB42- <i>OSH6</i>	OSH4.1D.MfeI
	AACCAACAATTGATGTCTCAATACGCAAGCTCAT
	OSH4.1302U.XhoI
pB42- <i>OSH7</i>	AACCAACTCGAGTTACAAAACAATTTCTTTTCTTC
	OSH5.1D.EcoRI
	AACCAAGAATTCATGTCTCAACACGCAAGCTCATCTTC
pB42- <i>OSH6</i>	OSH5.1305U.XhoI
	AACCAACTCGAGTTATATAGTAATTTCTGTTCTCCCTCATC
	OSH6.1D.EcoRV.2
pB42- <i>OSH7</i>	AACCAAGATATCAATGGGCTCCAAAAACTGAC
	OSH6.1344U.XhoI
	AACCAACTCGAGCTATTGTTTTGCTGGGTTCTG
pB42- <i>OSH7</i>	OSH7.1D.SmaI.2
	AACCAACCCGGAATGGCTCTCAATAAACTAAAGAATATAC
	OSH7.1314U.XhoI
	AACCAACTCGAGCTAATTTCTTTGGATTCCATGC

Table 3. Oligonucleotides used in this study for plasmid construction (Continued)

Plasmids made in this study	Oligonucleotides
p111osh2-KKK*-HA	OSH2.-580D.EcoRI
	AACCAAGAATTCGACCTATAGATAGTATGCCCAATTG
	Osh2.KKK-AAA.U
	TCCTCCTAGGATCCACACCGCCTGTGCTTTCGCGTTGTAGACTTCGCCTGT
p111osh2-PPVP*-ORD4-HA	Osh2.Osh4.D
	CCATCTACTACAAAAAGAGTTGCGAAACCTTTGAACCCATTTCTAGGTGAG
	OSH2.3891U.R1
p33ERG6-OSH4-HA	ATACAAGTACCAGGAAAAAGCTCGCATAAAAAAGCGTGGAATTCGAGCTCGTTTAAAC
	Erg6.linker.Osh4D
	CGCCGAAACCCCTCCCAAACCTCCCAAGAAGCAACTCAAGCAGGGGCAGCAGGGGCAGCAGCAGGGGCAGCAGGGGCAGCAATGTCTCAATACGCAAGCTCATC
	Erg6-R1
p111ERG6	AAATAGGTATATATCGTGCCTTTATTTGAATCTTATTGATCTAGTGAATGAATTCGAGCTCGTTTAAAC
	Erg6.-500D.BamHI
	AACCAACCGGATCCGATGCAACAGGGTAAGATCAG
	Erg6.TD200.EcoRI
p111erg6-D152L	AACCAACCGATTCTGGTCGTTTGCCACGACATG
	Erg6.-500D.BamHI
	AACCAACCGGATTCGATGCAACAGGGTAAGATCAG
	Erg6.TD200.EcoRI
pGST-ORD2	AACCAACCGAATTCTGGTCGTTTGCCACGACATG Erg6-D152L.D
	OSH2.GST.ORD2.new.EcoRI
	AACCAAGAATTCCAAAGAAAGAAGATATTTACTCAAAG
	OSH2.3840U.XhoI
p33ERG6-OSH4-HA	AACCAACTCGAGTTAAAAATGTCACCACAATCTTTC
	Erg6.linker.Osh4D
	CGCCGAAACCCCTCCCAAACCTCCCAAGAAGCAACTCAAGCAGGGGCAGCAGGGGCAGCAGCAGGGGCAGCAGGGGCAGCAATGTCTCAATACGCAAGCTCATC
	Osh4.R1
	ATTAGTGCAACGGTAACAAGTTGTTACTTTATCGTTCTCCGAATTCGAGCTCGTTTAAAC

HA-tagged strain that for the nontagged strain. Labeling was performed with the lowest possible antibody concentration to obtain one gold per image to statistically study independent events. The GRP of the GFP-D4H was compared with the GRP for immunogolds decorating the different proteins reported previously (Encinar del Dedo et al., 2014; Fernández-Golbano et al., 2014; Idrissi et al., 2012; Idrissi et al., 2008).

#### Quantification and statistical analysis

Quantifications and kymographs were performed with ImageJ (1997–2016, W.S. Rasband, National Institutes of Health; <http://imagej.nih.gov/ij>). Average, standard deviation, and P values for

the two-sided Student's *t* test of statistically significant differences were calculated with Microsoft Excel. Data distribution was assumed to be normal, but this was not formally tested.

#### Online supplemental material

Fig. S1 shows a scheme of the GFP-D4H sterol probe, the effect on the Sla1-GFP cortical dynamics of the GFP-D4H probe expression, a scheme of the late ergosterol biosynthetic pathway, the controls showing that the GFP-D4H probe recognizes sterols in yeast, and the effect of different *sec* and *osh* mutants on the polarization of the GFP-D4H probe. Fig. S2 shows the QEM data on the localization of the GFP-D4H probe, the effect of FPM on

the GFP-D4H cortical patch intensity; the effects of Osh4 depletion on the GFP-D4H cortical patch intensity and numbers; kymographs of representative GFP-D4H cortical patches upon treatment with TBF, FPM, or OSW-1; effects of TBF and OSW-1 on control strains lacking Osh1 or Osh3; effect of 1-h treatment with OSW-1 on the polarity of GFP-D4H; representative GFP-D4H cortical patches of yeast expressing different *osh2* alleles; and the effects of *osh2* mutation on the PI4P and PI(4,5)P<sub>2</sub> PM levels. **Fig. S3** shows colocalization of Erg proteins, BODIPY staining of Erg6 patches, time lapse of Abp1-mCherry in cells expressing Erg27-GFP, control immunoprecipitations or Erg-GFP-expressing cells, pull-down of the ORD of Osh2 and Erg6-GFP, the effect of 2-h treatments of OSW-1 and FPM on the GFP-D4H staining, and complementation of the endocytic defect of an *osh2Δ* strain with different *OSH2* alleles and the *ERG6-OSH4* chimera. **Video 1** and **Video 2** show WT yeast expressing GFP-D4H. **Video 3** shows a 3D view of a section of a WT cell where GFP-D4H patches can be seen at the rims of cER. **Video 4** shows the dynamics of a GFP-D4H patch at the rim of the cER. **Video 5** shows a 3D view of a section of a WT cell where Erg6-mCherry can be observed in big perinuclear structures, which correspond to LDs, and small cortical patches, which correspond to ERSEs. **Video 6** shows colocalization of Erg6-mCherry and Erg27-GFP. **Video 7** and **Video 8** show colocalization of Erg6-mCherry and GFP-D4H at the cortex. **Video 9** shows a 3D view of a section of a WT cell demonstrating colocalization of Abp1-mCherry and Erg6-GFP. **Video 10** shows that Erg27-GFP cortical patches label endocytic hot spots.

## Acknowledgments

We acknowledge M. Muñiz, H. Riezman, and M. Molina for critical reading; Leica Microsystems for support of the Molecular Imaging Platform; and C. Roncero (Instituto de Biología Funcional y Genómica, Salamanca, Spain), M. Munson (University of Massachusetts Medical School, Worcester, MA), K. Kozminski (University of Virginia, Charlottesville, VA), W. Prinz (NIH, Bethesda, MD), O. Gallego (Universitat Pompeu Fabra, Barcelona, Spain), M. Molina (Universidad Autónoma de Madrid, Madrid, Spain), A. Pol (Universitat de Barcelona, Barcelona, Spain), R. Piper (University of Iowa, Iowa City, IA), and A. Minard (University of Iowa, Iowa City, IA) for sharing plasmids and reagents.

This study was financed by the Spanish "Ministerio de Economía Industria y Competitividad" (grant BFU2017-82959-P).

The authors declare no competing financial interests.

Author contributions: J. Encinar del Dedo contributed to conceptualization, execution, and analysis of most experiments. I.M. Fernández-Golbano performed and analyzed QEM and some fluorescence micrographs experiments and generated plasmids and strains. P. Meler performed two-hybrid and pull-downs assays. L. Pastor generated plasmids and strains and purified proteins. C. Ferrer-Orta helped with protein purification. E. Rebollo designed the fluorescence imaging methodology. M.I. Geli contributed to conceptualization and analysis, funding acquisition, and supervision; performed some fluorescence micrograph and biochemical experiments; and wrote the original draft.

Submitted: 4 October 2020

Revised: 27 May 2021

Accepted: 29 June 2021

## References

- Alfaro, G., J. Johansen, S.A. Dighe, G. Duamel, K.G. Kozminski, and C.T. Beh. 2011. The sterol-binding protein Kes1/Osh4p is a regulator of polarized exocytosis. *Traffic*. 12:1521–1536. <https://doi.org/10.1111/j.1600-0854.2011.01265.x>
- Antony, B., J. Bigay, and B. Mesmin. 2018. The Oxysterol-Binding Protein Cycle: Burning Off PI(4)P to Transport Cholesterol. *Annu. Rev. Biochem.* 87:809–837. <https://doi.org/10.1146/annurev-biochem-061516-044924>
- Baumann, N.A., D.P. Sullivan, H. Ohvo-Rekilä, C. Simonot, A. Pottekat, Z. Klaassen, C.T. Beh, and A.K. Menon. 2005. Transport of newly synthesized sterol to the sterol-enriched plasma membrane occurs via nonvesicular equilibration. *Biochemistry*. 44:5816–5826. <https://doi.org/10.1021/bi048296z>
- Beh, C.T., L. Cool, J. Phillips, and J. Rine. 2001. Overlapping functions of the yeast oxysterol-binding protein homologues. *Genetics*. 157:1117–1140. <https://doi.org/10.1093/genetics/157.3.1117>
- Bhattacharya, S., B.D. Esquivel, and T.C. White. 2018. Overexpression or Deletion of Ergosterol Biosynthesis Genes Alters Doubling Time, Response to Stress Agents, and Drug Susceptibility in *Saccharomyces cerevisiae*. *MBio*. 9:e01291-18. <https://doi.org/10.1128/mBio.01291-18>
- de Saint-Jean, M., V. Delfosse, D. Douguet, G. Chicanne, B. Payrastré, W. Bourguet, B. Antony, and G. Drin. 2011. Osh4p exchanges sterols for phosphatidylinositol 4-phosphate between lipid bilayers. *J. Cell Biol.* 195:965–978. <https://doi.org/10.1083/jcb.201104062>
- Dubreuil, B., E. Sass, Y. Nadav, M. Heidenreich, J.M. Georgeson, U. Weill, Y. Duan, M. Meurer, M. Schuldiner, M. Knop, and E.D. Levy. 2019. YeastRGB: comparing the abundance and localization of yeast proteins across cells and libraries. *Nucleic Acids Res.* 47(D1):D1245–D1249. <https://doi.org/10.1093/nar/gky941>
- Dulic, V., M. Egerton, I. Elguindi, S. Raths, B. Singer, and H. Riezman. 1991. Yeast endocytosis assays. *Methods Enzymol.* 194:697–710. [https://doi.org/10.1016/0076-6879\(91\)94051-D](https://doi.org/10.1016/0076-6879(91)94051-D)
- Encinar del Dedo, J., F.Z. Idrissi, Y. Arnáiz-Pita, M. James, E. Dueñas-Santero, S. Orellana-Muñoz, F. del Rey, V. Sirotkin, M.I. Geli, and C.R. Vázquez de Aldana. 2014. Eng2 is a component of a dynamic protein complex required for endocytic uptake in fission yeast. *Traffic*. 15:1122–1142. <https://doi.org/10.1111/tra.12198>
- Encinar Del Dedo, J., F.Z. Idrissi, I.M. Fernández-Golbano, P. Garcia, E. Rebollo, M.K. Krzyzanowski, H. Grötsch, and M.I. Geli. 2017. ORP-Mediated ER Contact with Endocytic Sites Facilitates Actin Polymerization. *Dev. Cell*. 43:588–602.e6. <https://doi.org/10.1016/j.devcel.2017.10.031>
- Fang, M., B.G. Kearns, A. Gedvilaite, S. Kagiwada, M. Kearns, M.K. Fung, and V.A. Bankaitis. 1996. Kes1p shares homology with human oxysterol binding protein and participates in a novel regulatory pathway for yeast Golgi-derived transport vesicle biogenesis. *EMBO J.* 15:6447–6459. <https://doi.org/10.1002/j.1460-2075.1996.tb01036.x>
- Fernández-Golbano, I.M., F.Z. Idrissi, J.P. Giblin, B.L. Grosshans, V. Robles, H. Grötsch, M.M. Borrás, and M.I. Geli. 2014. Crosstalk between PI(4,5)P<sub>2</sub> and CK2 modulates actin polymerization during endocytic uptake. *Dev. Cell*. 30:746–758. <https://doi.org/10.1016/j.devcel.2014.07.020>
- Geli, M.I., and H. Riezman. 1996. Role of type I myosins in receptor-mediated endocytosis in yeast. *Science*. 272:533–535. <https://doi.org/10.1126/science.272.5261.533>
- Geli, M.I., R. Lombardi, B. Schmelzl, and H. Riezman. 2000. An intact SH3 domain is required for myosin I-induced actin polymerization. *EMBO J.* 19:4281–4291. <https://doi.org/10.1093/emboj/19.16.4281>
- Gietz, R.D., and A. Sugino. 1988. New yeast-Escherichia coli shuttle vectors constructed with in vitro mutagenized yeast genes lacking six-base pair restriction sites. *Gene*. 74:527–534. [https://doi.org/10.1016/0378-1119\(88\)90185-0](https://doi.org/10.1016/0378-1119(88)90185-0)
- Grosshans, B.L., H. Grötsch, D. Mukhopadhyay, I.M. Fernández, J. Pfannstiel, F.Z. Idrissi, J. Lechner, H. Riezman, and M.I. Geli. 2006. TEDS site phosphorylation of the yeast myosins I is required for ligand-induced but not for constitutive endocytosis of the G protein-coupled receptor Ste2p. *J. Biol. Chem.* 281:11104–11114. <https://doi.org/10.1074/jbc.M508933200>
- Grötsch, H., J.P. Giblin, F.Z. Idrissi, I.M. Fernández-Golbano, J.R. Collette, T.M. Newpher, V. Robles, S.K. Lemmon, and M.I. Geli. 2010.

- Calmodulin dissociation regulates Myo5 recruitment and function at endocytic sites. *EMBO J.* 29:2899–2914. <https://doi.org/10.1038/emboj.2010.159>
- Gyuris, J., E. Golemis, H. Chertkov, and R. Brent. 1993. Cdi1, a human G1 and S phase protein phosphatase that associates with Cdk2. *Cell.* 75:791–803. [https://doi.org/10.1016/0092-8674\(93\)90498-F](https://doi.org/10.1016/0092-8674(93)90498-F)
- Idrissi, F.Z., H. Grötsch, I.M. Fernández-Golbano, C. Presciatto-Baschong, H. Riezman, and M.I. Geli. 2008. Distinct acto/myosin-I structures associate with endocytic profiles at the plasma membrane. *J. Cell Biol.* 180:1219–1232. <https://doi.org/10.1083/jcb.200708060>
- Idrissi, F.Z., A. Blasco, A. Espinal, and M.I. Geli. 2012. Ultrastructural dynamics of proteins involved in endocytic budding. *Proc. Natl. Acad. Sci. USA.* 109:E2587–E2594. <https://doi.org/10.1073/pnas.1202789109>
- Inoue, M., S.H. Chiang, L. Chang, X.W. Chen, and A.R. Saltiel. 2006. Compartmentalization of the exocyst complex in lipid rafts controls Glut4 vesicle tethering. *Mol. Biol. Cell.* 17:2303–2311. <https://doi.org/10.1091/mbc.e06-01-0030>
- Ito, H., Y. Fukuda, K. Murata, and A. Kimura. 1983. Transformation of intact yeast cells treated with alkali cations. *J. Bacteriol.* 153:163–168. <https://doi.org/10.1128/jb.153.1.163-168.1983>
- Johansen, J., G. Alfaro, and C.T. Beh. 2016. Polarized Exocytosis Induces Compensatory Endocytosis by Sec4p-Regulated Cortical Actin Polymerization. *PLoS Biol.* 14:e1002534. <https://doi.org/10.1371/journal.pbio.1002534>
- Johnson, B.B., P.C. Moe, D. Wang, K. Rossi, B.L. Trigatti, and A.P. Heuck. 2012. Modifications in perfringolysin O domain 4 alter the cholesterol concentration threshold required for binding. *Biochemistry.* 51:3373–3382. <https://doi.org/10.1021/bi3003132>
- Joshi, A.S., B. Nebenfuhr, V. Choudhary, P. Satpute-Krishnan, T.P. Levine, A. Golden, and W.A. Prinz. 2018. Lipid droplet and peroxisome biogenesis occur at the same ER subdomains. *Nat. Commun.* 9:2940. <https://doi.org/10.1038/s41467-018-05277-3>
- Klemm, R.W., C.S. Ejsing, M.A. Surma, H.J. Kaiser, M.J. Gerl, J.L. Sampaio, Q. de Robillard, C. Ferguson, T.J. Proszynski, A. Shevchenko, and K. Simons. 2009. Segregation of sphingolipids and sterols during formation of secretory vesicles at the trans-Golgi network. *J. Cell Biol.* 185:601–612. <https://doi.org/10.1083/jcb.200901145>
- Koselny, K., N. Mutlu, A.Y. Minard, A. Kumar, D.J. Krysan, and M. Wellington. 2018. A Genome-Wide Screen of Deletion Mutants in the Filamentous *Saccharomyces cerevisiae* Background Identifies Ergosterol as a Direct Trigger of Macrophage Pyroptosis. *MBio.* 9:9. <https://doi.org/10.1128/mBio.01204-18>
- Kozminski, K.G., G. Alfaro, S. Dighe, and C.T. Beh. 2006. Homologues of oxysterol-binding proteins affect Cdc42p- and Rho1p-mediated cell polarization in *Saccharomyces cerevisiae*. *Traffic.* 7:1224–1242. <https://doi.org/10.1111/j.1600-0854.2006.00467.x>
- Kvam, E., and D.S. Goldfarb. 2004. Nvj1p is the outer-nuclear-membrane receptor for oxysterol-binding protein homolog Osh1p in *Saccharomyces cerevisiae*. *J. Cell Sci.* 117:4959–4968. <https://doi.org/10.1242/jcs.01372>
- Laemmli, U.K. 1970. Cleavage of structural proteins during the assembly of the head of bacteriophage T4. *Nature.* 227:680–685. <https://doi.org/10.1038/227680a0>
- Levine, T.P., and S. Munro. 2001. Dual targeting of Osh1p, a yeast homologue of oxysterol-binding protein, to both the Golgi and the nucleus-vacuole junction. *Mol. Biol. Cell.* 12:1633–1644. <https://doi.org/10.1091/mbc.12.6.1633>
- Li, X., M.P. Rivas, M. Fang, J. Marchena, B. Mehrotra, A. Chaudhary, L. Feng, G.D. Prestwich, and V.A. Bankaitis. 2002. Analysis of oxysterol binding protein homologue Kes1p function in regulation of Sec14p-dependent protein transport from the yeast Golgi complex. *J. Cell Biol.* 157:63–77. <https://doi.org/10.1083/jcb.200201037>
- Ling, Y., S. Hayano, and P. Novick. 2014. Osh4p is needed to reduce the level of phosphatidylinositol-4-phosphate on secretory vesicles as they mature. *Mol. Biol. Cell.* 25:3389–3400. <https://doi.org/10.1091/mbc.e14-06-1087>
- Maeda, K., K. Anand, A. Chiapparino, A. Kumar, M. Poletto, M. Kaksonen, and A.C. Gavin. 2013. Interactome map uncovers phosphatidylserine transport by oxysterol-binding proteins. *Nature.* 501:257–261. <https://doi.org/10.1038/nature12430>
- Maekawa, M. 2017. Domain 4 (D4) of Perfringolysin O to Visualize Cholesterol in Cellular Membranes—The Update. *Sensors (Basel).* 17:504. <https://doi.org/10.3390/s17030504>
- Marcireau, C., M. Guilloton, and F. Karst. 1990. In vivo effects of fenpropimorph on the yeast *Saccharomyces cerevisiae* and determination of the molecular basis of the antifungal property. *Antimicrob. Agents Chemother.* 34:989–993. <https://doi.org/10.1128/AAC.34.6.989>
- Marek, M., V. Vincenzetti, and S.G. Martin. 2020. Sterol biosensor reveals LAM-family Ltc1-dependent sterol flow to endosomes upon Arp2/3 inhibition. *J. Cell Biol.* 219:e202001147. <https://doi.org/10.1083/jcb.202001147>
- Menon, A.K. 2018. Sterol gradients in cells. *Curr. Opin. Cell Biol.* 53:37–43. <https://doi.org/10.1016/j.ceb.2018.04.012>
- Mesmin, B., B. Antonny, and G. Drin. 2013. Insights into the mechanisms of sterol transport between organelles. *Cell. Mol. Life Sci.* 70:3405–3421. <https://doi.org/10.1007/s00018-012-1247-3>
- Mesmin, B., J. Bigay, J. Polidori, D. Jamecna, S. Lacas-Gervais, and B. Antonny. 2017. Sterol transfer, PI4P consumption, and control of membrane lipid order by endogenous OSBP. *EMBO J.* 36:3156–3174. <https://doi.org/10.15252/emboj.201796687>
- Mo, C., and M. Bard. 2005. A systematic study of yeast sterol biosynthetic protein-protein interactions using the split-ubiquitin system. *Biochim. Biophys. Acta.* 1737:152–160. <https://doi.org/10.1016/j.bbali.2005.11.002>
- Moser von Filseck, J., A. Čopič, V. Delfosse, S. Vanni, C.L. Jackson, W. Bourguet, and G. Drin. 2015a. INTRACELLULAR TRANSPORT. Phosphatidylserine transport by ORP/Osh proteins is driven by phosphatidylinositol 4-phosphate. *Science.* 349:432–436. <https://doi.org/10.1126/science.aab1346>
- Moser von Filseck, J., S. Vanni, B. Mesmin, B. Antonny, and G. Drin. 2015b. A phosphatidylinositol-4-phosphate powered exchange mechanism to create a lipid gradient between membranes. *Nat. Commun.* 6:6671. <https://doi.org/10.1038/ncomms7671>
- Mulholland, J., D. Preuss, A. Moon, A. Wong, D. Drubin, and D. Botstein. 1994. Ultrastructure of the yeast actin cytoskeleton and its association with the plasma membrane. *J. Cell Biol.* 125:381–391. <https://doi.org/10.1083/jcb.125.2.381>
- Munn, A.L., A. Heese-Peck, B.J. Stevenson, H. Pichler, and H. Riezman. 1999. Specific sterols required for the internalization step of endocytosis in yeast. *Mol. Biol. Cell.* 10:3943–3957. <https://doi.org/10.1091/mbc.10.11.3943>
- Nes, W.D., P. Jayasimha, W. Zhou, R. Kanagasabai, C. Jin, T.T. Jaradat, R.W. Shaw, and J.M. Bujnicki. 2004. Sterol methyltransferase: functional analysis of highly conserved residues by site-directed mutagenesis. *Biochemistry.* 43:569–576. <https://doi.org/10.1021/bi035257z>
- Nishimura, T., M. Gecht, R. Covino, G. Hummer, M.A. Surma, C. Klose, H. Arai, N. Kono, and C.J. Stefan. 2019. Osh Proteins Control Nanoscale Lipid Organization Necessary for PI(4,5)P<sub>2</sub> Synthesis. *Mol. Cell.* 75:1043–1057.e8. <https://doi.org/10.1016/j.molcel.2019.06.037>
- Prinz, W.A., A. Toulmay, and T. Balla. 2020. The functional universe of membrane contact sites. *Nat. Rev. Mol. Cell Biol.* 21:7–24. <https://doi.org/10.1038/s41580-019-0180-9>
- Raychaudhuri, S., Y.J. Im, J.H. Hurley, and W.A. Prinz. 2006. Nonvesicular sterol movement from plasma membrane to ER requires oxysterol-binding protein-related proteins and phosphoinositides. *J. Cell Biol.* 173:107–119. <https://doi.org/10.1083/jcb.200510084>
- Riezman, H. 1985. Endocytosis in yeast: several of the yeast secretory mutants are defective in endocytosis. *Cell.* 40:1001–1009. [https://doi.org/10.1016/0092-8674\(85\)90360-5](https://doi.org/10.1016/0092-8674(85)90360-5)
- Sambrook, J., E.F. Fritsch, and T. Maniatis. 1989. *Molecular Cloning: a Laboratory Manual*. Second edition. Cold Spring Harbor Laboratory Press
- Savinov, S.N., and A.P. Heuck. 2017. Interaction of Cholesterol with Perfringolysin O: What Have We Learned from Functional Analysis? *Toxins (Basel).* 9:381. <https://doi.org/10.3390/toxins9120381>
- Schneider, R., B. Brügger, R. Sandhoff, G. Zellnig, A. Leber, M. Lampl, K. Athenstaedt, C. Hrastnik, S. Eder, G. Daum, et al. 1999. Electrospray ionization tandem mass spectrometry (ESI-MS/MS) analysis of the lipid molecular species composition of yeast subcellular membranes reveals acyl chain-based sorting/remodeling of distinct molecular species en route to the plasma membrane. *J. Cell Biol.* 146:741–754. <https://doi.org/10.1083/jcb.146.4.741>
- Schulz, T.A., M.G. Choi, S. Raychaudhuri, J.A. Mears, R. Ghirlando, J.E. Hinshaw, and W.A. Prinz. 2009. Lipid-regulated sterol transfer between closely apposed membranes by oxysterol-binding protein homologues. *J. Cell Biol.* 187:889–903. <https://doi.org/10.1083/jcb.200905007>
- Smindak, R.J., L.A. Heckle, S.S. Chittari, M.A. Hand, D.M. Hyatt, G.E. Mantus, W.A. Sanfelippo, and K.G. Kozminski. 2017. Lipid-dependent regulation of exocytosis in *S. cerevisiae* by OSBP homolog (Osh) 4. *J. Cell Sci.* 130:3891–3906.



- Spang, A. 2015. Anniversary of the discovery of sec mutants by Novick and Schekman. *Mol. Biol. Cell.* 26:1783–1785. <https://doi.org/10.1091/mbc.E14-11-1511>
- Stefan, C.J., A.G. Manford, D. Baird, J. Yamada-Hanff, Y. Mao, and S.D. Emr. 2011. Osh proteins regulate phosphoinositide metabolism at ER-plasma membrane contact sites. *Cell.* 144:389–401. <https://doi.org/10.1016/j.cell.2010.12.034>
- Tarassov, K., V. Messier, C.R. Landry, S. Radinovic, M.M. Serna Molina, I. Shames, Y. Malitskaya, J. Vogel, H. Bussey, and S.W. Michnick. 2008. An in vivo map of the yeast protein interactome. *Science.* 320:1465–1470. <https://doi.org/10.1126/science.1153878>
- Tong, J., H. Yang, H. Yang, S.H. Eom, and Y.J. Im. 2013. Structure of Osh3 reveals a conserved mode of phosphoinositide binding in oxysterol-binding proteins. *Structure.* 21:1203–1213. <https://doi.org/10.1016/j.str.2013.05.007>
- Wach, A., A. Brachat, C. Alberti-Segui, C. Rebischung, and P. Philippsen. 1997. Heterologous HIS3 marker and GFP reporter modules for PCR-targeting in *Saccharomyces cerevisiae*. *Yeast.* 13:1065–1075. [https://doi.org/10.1002/\(SICI\)1097-0061\(19970915\)13:11<1065::AID-YEA159>3.0.CO;2-K](https://doi.org/10.1002/(SICI)1097-0061(19970915)13:11<1065::AID-YEA159>3.0.CO;2-K)
- Wang, H., Q. Ma, Y. Qi, J. Dong, X. Du, J. Rae, J. Wang, W.F. Wu, A.J. Brown, R.G. Parton, et al. 2019. ORP2 Delivers Cholesterol to the Plasma Membrane in Exchange for Phosphatidylinositol 4, 5-Bisphosphate (PI(4,5)P<sub>2</sub>). *Mol. Cell.* 73:458–473.e7. <https://doi.org/10.1016/j.molcel.2018.11.014>
- Wong, L.H., A.T. Gatta, and T.P. Levine. 2019. Lipid transfer proteins: the lipid commute via shuttles, bridges and tubes. *Nat. Rev. Mol. Cell Biol.* 20:85–101. <https://doi.org/10.1038/s41580-018-0071-5>
- Yu, J.W., J.M. Mendrola, A. Audhya, S. Singh, D. Keleti, D.B. DeWald, D. Murray, S.D. Emr, and M.A. Lemmon. 2004. Genome-wide analysis of membrane targeting by *S. cerevisiae* pleckstrin homology domains. *Mol. Cell.* 13:677–688. [https://doi.org/10.1016/S1097-2765\(04\)00083-8](https://doi.org/10.1016/S1097-2765(04)00083-8)

## Supplemental material

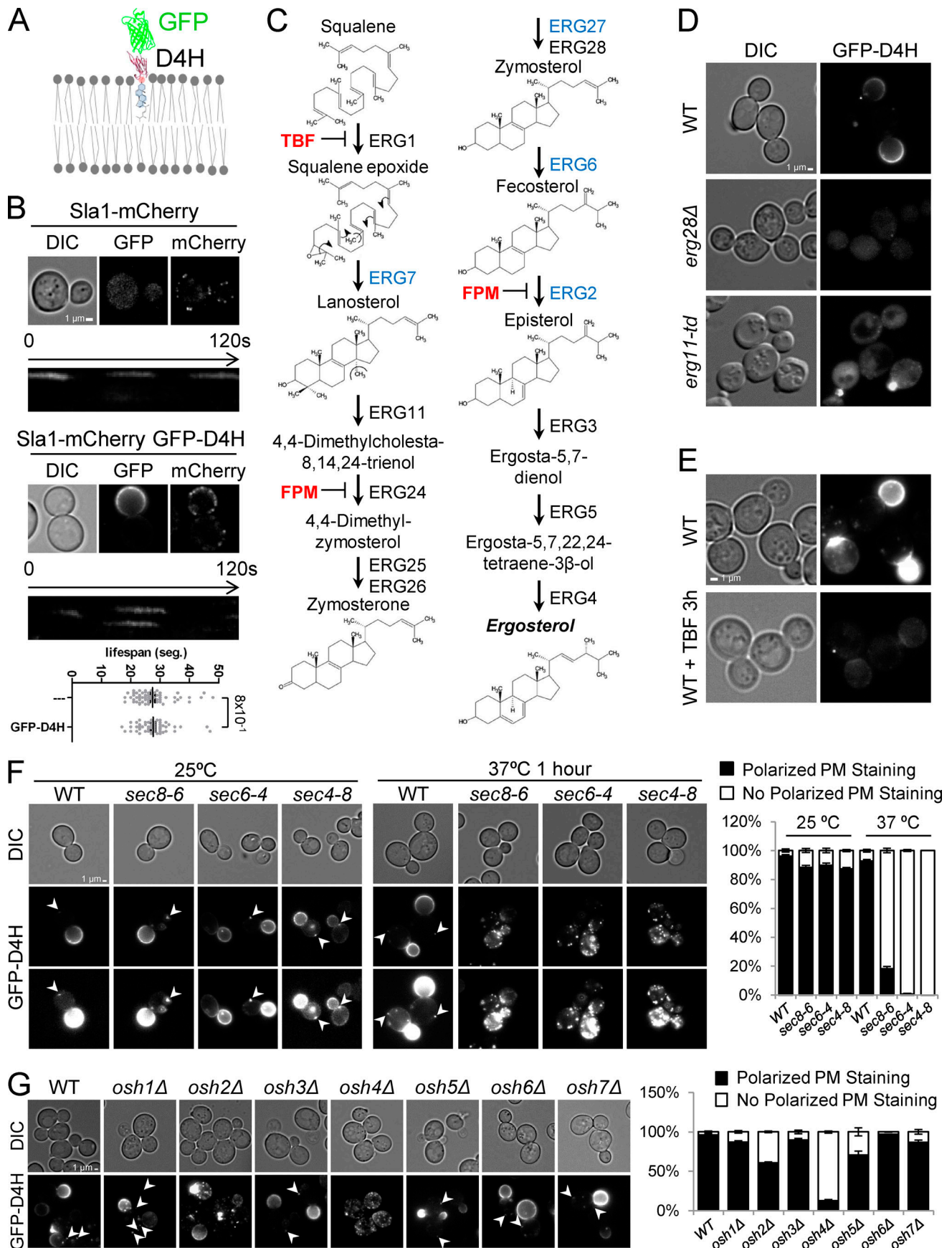


Figure S1. **Asymmetric distribution of GFP-D4H labeling in yeast.** **(A)** Scheme of the GFP-D4H probe that recognizes sterols. **(B)** Kymographs of time-lapse fluorescence movies of Sla1-mCherry cortical patches of WT cells expressing or not GFP-D4H. Images were taken every 1 s. A graph of average  $\pm$  SEM life span of Sla1-mCherry cortical patches with Student's *t* test *P* values is shown ( $n > 150$ ). **(C)** Ergosterol late biosynthetic pathway. Ergs localized at ERSESEs are shown in blue. Steps inhibited by TBF and FPM are indicated. **(D–G)** DIC and epifluorescence micrographs of the indicated strains expressing GFP-D4H, grown at 25°C or upon shift at 37°C for 1 h (F). Arrowheads point to vesicle-like structures. Graphs in F and G represent average  $\pm$  SEM frequencies of cells showing polarized staining.  $n > 100$  cells in three experiments.

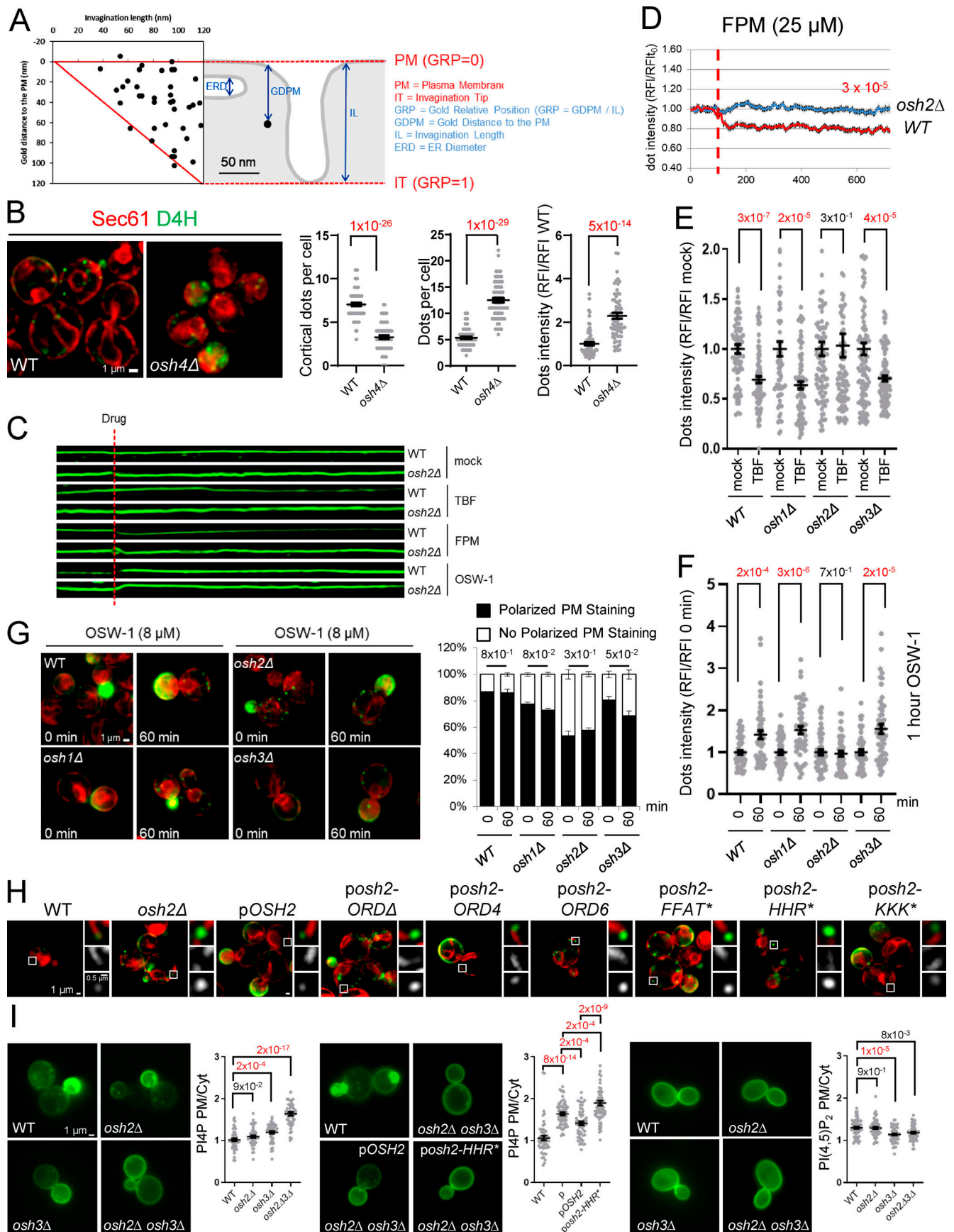


Figure S2. **Osh2 uses PI4P counter-transport to sustain sterol extraction from ERSEs.** **(A)** Graph representing the HA-GFP-D4H gold distance to the PM (GDPM) versus the length of the associated invagination (IL) for 40 endocytic invaginations. The GRP is calculated by dividing the GDPM by the IL. Red lines indicate the position of the PM (GRP = 0) and the position of the invagination tip (GRP = 1) as the invagination grows. An immuno-gold with  $GRP < 0.5$  is defined to be at the base of the invagination, with  $0.5 \leq GRP < 0.8$  at the invagination neck and  $GRP \geq 0.8$  at the invagination tip. The diagram on the right describes the parameters defined for each gold particle, cER, or invagination for a depicted invagination of  $IL = 150$  nm. **(B)** Merged epifluorescence micrographs of WT and *osh4Δ* cells expressing GFP-D4H and Sec61-mCherry. Graphs of average  $\pm$  SEM number of cortical GFP-D4H patches, total number of GFP-D4H foci, and their RFI normalized to the WT in the indicated strains, with the Student's *t* test P values, are shown. Significant differences are shown in red.  $n > 45$  cells or patches in three experiments. **(C)** Kymographs of GFP-D4H cortical patches in WT or *osh2Δ* cells either mock treated or treated with the indicated drugs. Pictures were taken every 5 s for 12 min, and drugs were added 2 min after initiation of the experiment (red line). **(D)** Time course of cortical GFP-D4H patch RFI, normalized to time 0, in WT or *osh2Δ* cells treated with FPM. The drug was added 2 min after initiation of the experiment (red dashed line). The Student's *t* test P value in the last time recorded is indicated ( $n \geq 10$ ). **(E)** Graph of average  $\pm$  SEM with Student's *t* test P values of the GFP-D4H cortical patch intensity for the indicated strains, 1 h upon incubation with TBF or mock treated. RFI is normalized to the average of the mock-treated sample. **(F)** Graph of average  $\pm$  SEM with Student's *t* test P values of cortical GFP-D4H patch intensity of the indicated strains, before (0 min) or after 1-h treatment (60 min) with OSW-1. RFI is normalized to the average of the 0-min sample. Significant differences are in red. **(G)** Merged epifluorescence micrographs of the indicated strains expressing GFP-D4H and Sec61-mCherry before (0 min) or after 1-h treatment with OSW-1. The graph indicates average  $\pm$  SEM of the percentage of cells with polarized GFP-D4H staining in the indicated strains. **(H)** Merged epifluorescence micrographs of WT or *osh2Δ* strains bearing either the empty plasmid (*osh2Δ*) or plasmids encoding the indicated *OSH2* alleles expressing GFP-D4H and Sec61-mCherry. Individual channels and the merged micrographs of magnified areas showing GFP-D4H cortical patches associated with cER rims are shown. **(I)** Epifluorescence micrographs of yeast expressing PI4P (GFP-Osh2-PH) and PI(4,5)P<sub>2</sub> probes (GFP-2xPH-PLCδ; Yu et al., 2004) in the indicated strains, and graphs of the average  $\pm$  SEM with Student's *t* test P values of the relative PM/cytosolic (Cyt.) RFI for the corresponding probes and indicated strain backgrounds.

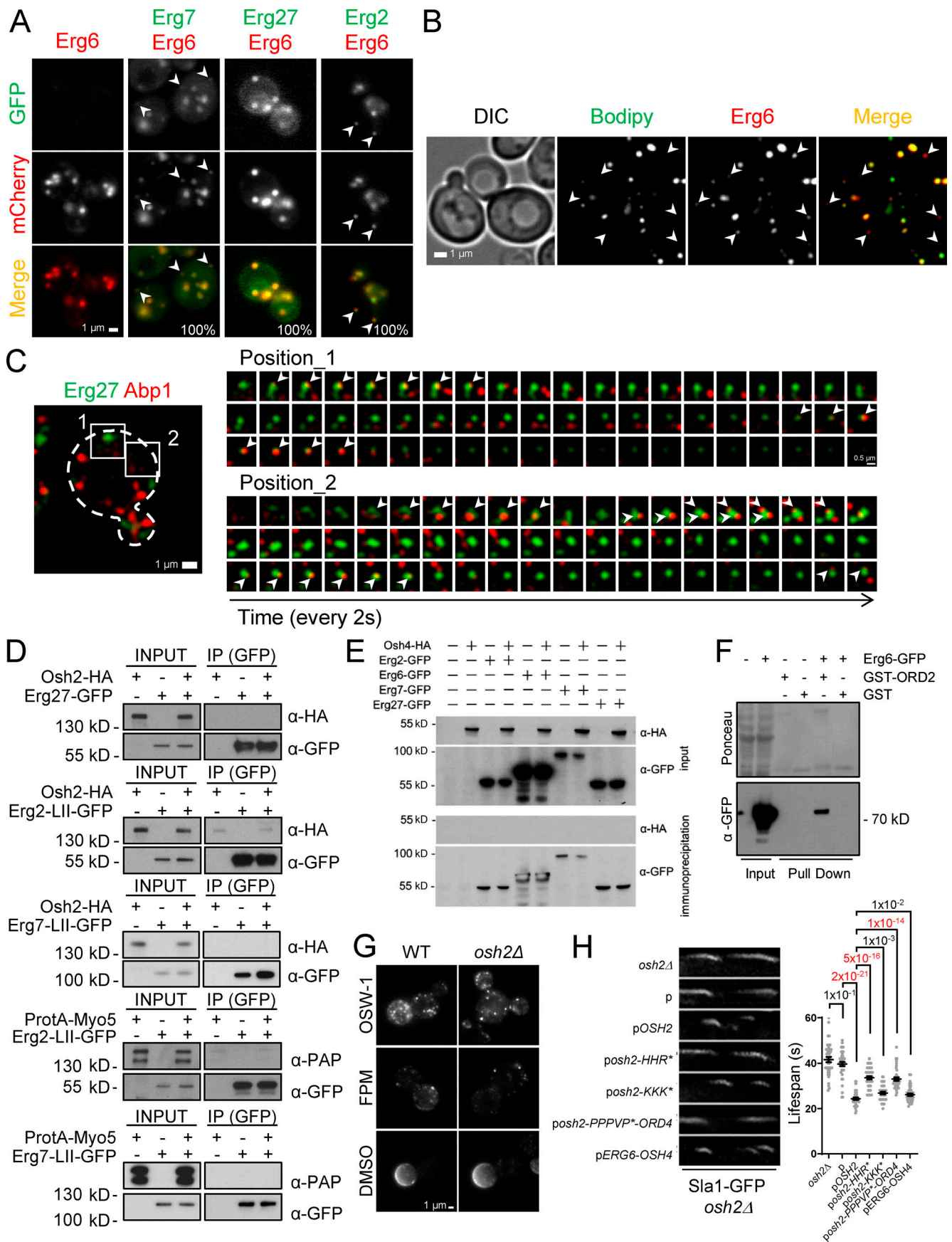


Figure S3. **A subset of Erg proteins labels endocytic hot spots.** **(A)** Individual channels and merged epifluorescence micrographs of cells expressing the indicated Ergs tagged with mCherry (red) and/or GFP (green). **(B)** DIC, individual channels, and merged FMs of cells expressing Erg6-mCherry, stained with BODIPY (0.5  $\mu$ g/ml). Arrowheads indicate cortical Erg6-mCherry dots with no detectable BODIPY signal. **(C)** Merged FMs of cells expressing Erg27-GFP and Abp1-mCherry, and merge of a time lapse of the indicated magnified areas showing repetitive assembly of endocytic actin (arrowheads) at ERSEs. **(D and E)** Immunoblots of anti-GFP agarose precipitates (IP [GFP]) from yeast expressing the indicated protein A (ProtA), GFP, or HA-tagged proteins (+) or nontagged versions (-), probed for HA ( $\alpha$ -HA), Protein A (PAP), or GFP ( $\alpha$ -GFP). 10  $\mu$ g total protein was loaded in the inputs. **(F)** Ponceau red staining (upper panel) and immunoblot (lower panel) of glutathione-Sepharose pull-downs of GST or GST fused to the Osh2 ORD, expressed and purified from *E. coli*, and incubated with yeast extracts expressing Erg6-GFP (+) or the untagged Erg6 (-), probed for GFP ( $\alpha$ -GFP). **(G)** Epifluorescence micrographs of the indicated yeast strains expressing GFP-D4H treated for 2 h with DMSO, TBF, FPM, or OSW-1. **(H)** Average  $\pm$  SEM life span and Student's *t* test *P* values of Sla1-GFP cortical patch life spans in *osh2 $\Delta$*  cells expressing the indicated *OSH2* alleles from centromeric plasmids. Significant differences are in red ( $n > 150$ ). Kymographs of the time-lapse fluorescence movies for each experimental condition are shown. Images were taken every 0.5 s.

Video 1. **Time-lapse movie of a WT cell expressing GFP-D4H.** The video shows the DIC and GFP channels. Images were taken every 30 s during 120 min.

Video 2. **Time-lapse movie of a WT cell expressing GFP-D4H.** The video shows the GFP channel. Images were taken every 5 s during 10 min.

Video 3. **3D movie of a section of a WT cell expressing the ER marker Sec61-mCherry and GFP-D4H.** The video shows the merge of individual channels. Sec61-mCherry and GFP-D4H are depicted in red and green, respectively.

Video 4. **Time-lapse movie of a cortical patch of a WT cell expressing the ER marker Sec61-mCherry and the GFP-D4H.** The video shows the merge and the individual channels. Images were taken every 5 s during 45 s.

Video 5. **3D movie of a section of a WT cell expressing the ER marker Sec61-GFP and Erg6-mCherry.** The video shows the merge of individual channels. A movie with enhanced brightness is shown to evidence the small cortical Erg6-mCherry patches. Sec61-GFP and Erg6-mCherry are depicted in green and red, respectively.

Video 6. **Time-lapse movie of a WT cell expressing Erg6-mCherry and Erg27-GFP.** The video shows the merge of individual channels. Images were taken every 2 s during 2 min.

Video 7. **Time-lapse movie of a cortical patch of a cell expressing Erg6-mCherry and GFP-D4H.** The video shows the merge of individual channels. Images were taken every 2 s during 2 min.

Video 8. **Time-lapse movie of a cortical patch of a cell expressing Erg6-mCherry and GFP-D4H.** The video shows the merge of individual channels. Images were taken every 2 s during 40 s.

Video 9. **3D movie of a section of a WT cell expressing the actin marker Abp1-mCherry and Erg6-GFP.** The video shows the merge and the individual channels. Erg6-GFP and Abp1-mCherry are depicted in green and red, respectively.

Video 10. **Time-lapse movie of a cortical patch of a yeast expressing Erg27-GFP and Abp1-mCherry.** The video shows the merge of individual channels. Images were taken every 2 s during 2 min. The movie corresponds to position 1 in [Fig. S3 C](#).